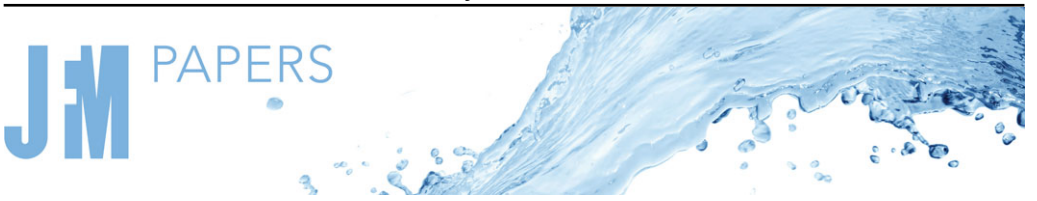
*J. Fluid Mech.* (2025), *vol.* 1010, A25, doi:10.1017/jfm.2025.231



# Turbulent/non-turbulent interface in polymer-laden jets

**Sheng-Hong Peng**[1,2], **Xi-Ran Liu**[1], **Yi-Bao Zhang**[1,3] and **Heng-Dong Xi**[1]

[1]Institute of Extreme Mechanics and School of Aeronautics, Northwestern Polytechnical University, Xi'an 710072, PR China

[2]BYD Auto Company Limited, Xi'an 710072, PR China

[3]Center for Combustion Energy, Key Laboratory for Thermal Science and Power Engineering of Ministry of Education, Department of Energy and Power Engineering, Tsinghua University, Beijing 100084, PR China

**Corresponding authors:** Yi-Bao Zhang, zhangyibao@mail.tsinghua.edu.cn; Heng-Dong Xi, hengdongxi@nwpu.edu.cn

(Received 26 January 2024; revised 2 February 2025; accepted 23 February 2025)

We present an experimental study on the effects of polymer additives on the turbulent/non-turbulent interface (TNTI) in a fully developed round water jet. The Reynolds number based on the jet diameter is fixed at $Re = 7075$. The Weissenberg number $Wi$ ranges from 24 to 86. We employ time-resolved simultaneous particle image velocimetry and laser-induced fluorescence measurements to investigate the local entrainment and engulfment process along the TNTI in two regimes: entrainment transition and enhancement regimes. In polymer-laden jets, the TNTI fluctuates more intermittently in the radial direction and more ambient fluid can be engulfed into the turbulent region due to the augmented large scale motion. Though the contribution of engulfment to the total flux increases with $Wi$, engulfment is still not the major contribution to the entrainment in polymer-laden jets. We further show that the local entrainment velocity is increased in both regimes compared with the pure water jet, due to two contributions: polymer elastic stress and the more intermittent character of the TNTI. In the entrainment transition regime, we observe smaller fractal dimension and shorter length of TNTI compared with the Newtonian case, consistent with previous numerical simulations (Abreu *et al. J. Fluid Mech.* vol. 934, 2022, A36); whereas those in the enhancement regime remain largely unchanged. The difference between the two regimes results from the fact that the jet flow decays in the streamwise direction. In the entrainment transition regime, turbulence intensity is strong enough to significantly stretch the polymers, resulting in a smoother TNTI in the inertial range. However, in the entrainment enhancement regime, the polymer's feedback is not strong enough to alter the fractal dimension due to the low elasticity. The above mentioned differences of entrainment velocity and TNTI in the entrainment reduction/transition and enhancement regimes also explain the reduced and enhanced spreading rate of the

https://doi.org/10.1017/jfm.2025.231 Published online by Cambridge University Press

© The Author(s), 2025. Published by Cambridge University Press.

viscoelastic jet observed in previous numerical simulations and experiments (Guimarães *et al. J. Fluid Mech.* 2020, vol. 899, A11; Peng *et al. Phys. Fluids*, 2023, vol. 35, 045110).

**Key words:** mixing enhancement, jets, polymers

## 1. Introduction

The addition of minute amounts of long-chain flexible polymers to fluid flow can drastically change the flow behaviours, such as reducing the drag in pipe/channel flow (Bailey & Koleske 1976; White & Mungal 2008; Xi 2019), attenuating flow-induced noise in underwater vehicles (Polmar & Moore 2004), reducing the risk of explosion when the oil tank is impacted during an air crash event (Wei *et al.* 2015) and inhibiting the energy transfer from the large to small scales (Ouellette *et al.* 2009; Xi *et al.* 2013; Zhang *et al.* 2021). However, compared with polymer drag reduction, the effects of polymers on turbulent transport and mixing have received less attention (Gupta *et al.* 2005; Vaithianathan *et al.* 2007; Liberzon *et al.* 2009; Cocconi *et al.* 2017; Boffetta *et al.* 2010). Recently, there has been growing interest in investigating the impact of polymers on jet flows (Guimarães *et al.* 2020, 2022, 2023; Peng *et al.* 2023; Soligo & Rosti 2023; Yamani *et al.* 2023; Guimarães *et al.* 2024), which is a canonical configuration for studying turbulent transport and mixing.

In Newtonian jets, the turbulent core is surrounded by the non-turbulent fluid, separated by a sharp and highly convoluted boundary called the turbulent/non-turbulent interface (TNTI) (da Silva *et al.* 2014*a*). The non-turbulent fluid is transported across the TNTI and becomes part of the turbulent region, resulting in an increase of mass flux with downstream distance. There was a debate on whether this entrainment process is dominated by large-scale engulfment or small-scale viscous nibbling along the TNTI (Roshko 1976; Mathew & Basu 2002; Holzner *et al.* 2008; Jahanbakhshi & Madnia 2016). However, it has been realised that entrainment is a multi-scale process with a scale-independent mean mass flux across the TNTI (Meneveau & Sreenivasan 1990; de Silva *et al.* 2013; Mistry *et al.* 2016). The entrainment velocity at small scales is small but is balanced by a large surface area, while the entrainment velocity at large scales is large but is balanced by a smoother surface area (Philip *et al.* 2014; Mistry *et al.* 2016). Therefore, the local entrainment velocity along the TNTI and the interface area are combined to determine the entrainment rate.

In polymer-laden jets, most of the previous literatures studied the instability of viscoelastic jet (Ray & Zaki 2014, 2015; Yamani *et al.* 2021; Soligo & Rosti 2023; Yamani *et al.* 2023), or the entrainment from a global view, i.e. the jet half-width and mean centreline velocity (see Guimarães *et al.* 2020, Peng *et al.* 2023 and references therein). Only in recent years, with the advancement of numerical simulation and experimental measurement technique, has it become possible to study the local entrainment process by tracking the TNTI. Guimarães *et al.* (2020, 2022) simulated the momentum equation coupled with finitely extensible nonlinear elastic with Peterlin closure model in planar jet and wake flows. They found that the entrainment rate is suppressed in the very near field and developed a new scaling theory in this entrainment reduction regime. Further downstream, the spreading rate is enhanced compared with the Newtonian case (Guimarães *et al.* 2022), which was later observed in our experiment (Peng *et al.* 2023). Abreu *et al.* (2022) numerically studied the entrainment in a shear-free turbulence. They found that polymer elastic stress accelerates the propagation of TNTI, resulting in an increase the mean entrainment velocity. However, the interface area in the viscoelastic case is much smaller than that in the Newtonian case due to the suppression of small-scale structures.



https://doi.org/10.1017/jfm.2025.231 Published online by Cambridge University Press

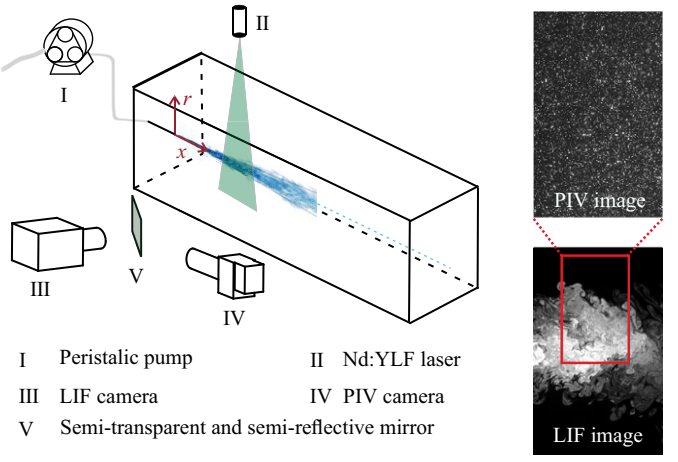



Figure 1. Schematic of the experimental set-up for jet flow and optical configuration for combined PIV and LIF measurements.

The combined effect is that the entrainment rate is reduced in the viscoelastic fluid. Guimarães *et al.* (2023) studied the influence of viscoelasticity on the evolution of the perturbations at the linear and nonlinear regimes of perturbation growth of a submerged jet. Guimarães *et al.* (2024) reported that the polymer conformation can be divided into highly stretched and nearly coiled regimes with distinct turbulence characteristics.

From the above discussion, it is clear that experimental study of the local entrainment process in a viscoelastic jet is still lacking. With the development of the 'graphical' approach to track the TNTI (Wolf *et al.* 2012), investigation of local entrainment in experiments is possible (Mistry *et al.* 2016; Long *et al.* 2022). This paper aims to experimentally elucidate the entrainment mechanism of the polymer-laden jet from the perspective of TNTI. The paper is divided into four sections. Section 2 presents the experimental apparatus, measurement methodology, and the method for detecting TNTI and determining the entrainment velocity. Section 3 discusses the effects of polymers on the turbulence characteristics. Section 4 analyses the engulfment and local entrainment process of the polymer-laden jet. Finally, our results are summarised in § 5.

## 2. Experimental set-up and methods

### 2.1. *Apparatus*

The jet facility used in the current study has been described in detail by Peng *et al.* (2023), here we only show the key features of the set-up. Figure 1 presents a schematic of the experimental set-up. The jet was generated in a 1.7 m long plexiglass rectangular tank with a cross-section of 0.3 m $\times$ 0.4 m, filled with 178 litres of deionised water or premixed aqueous polymer solution to a depth of 0.35 m. The jet fluid was introduced into the tank via a small circular pipe (nozzle) with an inner diameter ($D$) of 3 mm and a length of 200 mm. A separate reservoir, containing dyed deionised water/polymer solution, was utilised to supply the jet, hereafter referred to as pure water jet and polymer-laden jet, respectively. For the experiments using polymer solution, both the jet and the fluid in the tank are premixed aqueous polymer solutions with the same concentration. We employed two peristaltic pumps (Cole-Parmer, MasterFlex) to pump the fluid in the reservoir to the nozzle, thereby avoiding polymer degradation due to strong shear force if a mechanical pump is used. Pulsation dampeners (not shown in figure 1) were connected between the jet



https://doi.org/10.1017/jfm.2025.231 Published online by Cambridge University Press

pipe and pumps to minimise pulsations induced by idler wheels of peristaltic pump. The mean velocity at the nozzle exit $U_e$ (volume flow rate divided by the cross-sectional area of the nozzle) is 2.36 ms$^{-1}$ and the corresponding Reynolds number is $Re = U_e D/\nu = 7075$, where $\nu$ is the kinematic viscosity of the fluid. We note that at this $Re$, the pipe flow is turbulent. The flow rate was carefully calibrated for each experiment, with a maximum deviation of less than 1 %. The pipe was positioned $500D$ away from the tank's end wall, and no backflow was observed during the simultaneous PIV (particle image velocimetry) and LIF (laser-induced fluorescence) measurements, which lasted approximately eight seconds. Prior to measurement, the fluid temperature in the tank was regulated to 22 °C by an immersed copper tube coil with circulating water from a refrigerated circulator (Polyscience 9702). The fluid temperature inside the tank was monitored with a PT100 temperature sensor and was found to vary by less than $\pm 0.1$ °C during the measurement, thus the temperature variation that could affect the physical properties of the polymer solution is minimised.

For polymeric fluid flows, two additional control parameters are relevant: polymer concentration $\phi$ and Weissenberg number $Wi$. The polymer solution was prepared to a given concentration following the same protocol as of Zhang *et al.* (2021) and Peng *et al.* (2023). In a polymer-laden jet, the exit Weissenberg number is defined as $Wi = 2U_e\tau_p/D$, which is the ratio of the polymer's longest relaxation time $\tau_p$ to the characteristic time of the jet at the exit $D/2U_e$. The polymer relaxation time $\tau_p$ is estimated from the Zimm model $\tau_p = R_g^3\mu/(k_B T)$, where $R_g = N^{3/5}l$ is the equilibrium radius of gyration of the polymer, $N$ is the number of monomers, $l$ is the length of a monomer, $\mu$ is the dynamic viscosity of the solvent, $K_B$ is the Boltzmann constant and $T$ is the temperature. The polymer used in this study is polyethylene oxide (PEO, Sigma–Aldrich) with different molecular weights $M_w$. The monomer of PEO is $CH_2CH_2O$, and its molecular weight and length $l$ are 44 and 0.44 nm, respectively. We here take PEO with $M_w = 5 \times 10^6$ as an example, it consists of $N \approx 1.1 \times 10^6$ monomers, with a radius of gyration $R_g = N^{3/5}a = 475$ nm. When subjected to low-shear flow, the polymer molecule remains coiled and does not affect the flow. However, when the shear is strong enough, i.e. $Wi$ is larger than a critical value, the polymer molecule will be unravelled along the major stretching direction and in turn affects the flow. In the fully stretched state, the maximum length of the macromolecular is $R_{max} = Na \approx 50\,000$ nm, which is 100 times larger than that in the coiled state.

### 2.2. *Time-resolved simultaneous PIV and LIF measurements*

The measurement of local entrainment velocity along the TNTI requires the knowledge of velocity and scalar concentration fields at the same time, both of which need to be time-resolved. We employed two-dimensional PIV (LaVision) and LIF to measure the velocity and scalar concentration in the streamwise-radial plane ($x$–$r$) (see figure 1). A twin Nd:YLF high-speed laser, with wavelength 527 nm, maximum frequency 10 kHz and maximum energy 30 mJ per pulse, was used to illuminate both the seeding particles and the fluorescent dye. The laser beam, after passing through a series of cylindrical lenses, formed a laser sheet of approximately 0.5 mm in thickness. The tracer particles used were hollow spherical glass particles with a density of $1.1 \times 10^3$ kgm$^{-3}$ and an average diameter of 10 μm. Rhodamine 6G (Maikun) was used as the fluorescent dye for LIF measurement, with maximum light absorption at 525 nm and fluorescence emission peaked at 555 nm (Crimaldi 2008). The molecular diffusivity of rhodamine 6G in water is $\kappa = 2.8 \times 10^{-10}$ m$^2$s$^{-1}$ (Nie *et al.* 1994), yielding a Schmidt number $Sc = \nu/\kappa \approx 3400$.



https://doi.org/10.1017/jfm.2025.231 Published online by Cambridge University Press

| | PIV | LIF |
|---|---|---|
| Camera resolution | 1600 × 2560 pixels | 800 × 1280 pixels |
| Lenses | 200 mm Nikkor | 100 mm Tokina |
| Aperture of the lenses | $f^{\#} = 8$ | $f^{\#} = 8$ |
| Sampling rate | 400 Hz | 400 Hz |
| Field of view $(x - r)$ | 38 mm × 61 mm | 66 mm × 105 mm |
| Integration window | 24 × 24 pixels (75 % overlap) | — |
| Spatial resolution | 0.428 mm | 0.083 mm (single pixel) |
| | $3{-}7\eta$ | $0.6{-}1.4\eta$ |
| | — | $30{-}80\eta_B$ |

Table 1. Parameters for the PIV and LIF measurements. $\eta$ and $\eta_B$ denote the Kolmogorov and Batchelor length scales, respectively. These scales are estimated at the centreline for all the streamwise locations measured in the present study.

When the concentration of rhodamine 6G is smaller than 100 ppb (parts per billion by weight), the excited fluorescent light intensity is proportional to the concentration. The preparation of a rhodamine 6G solution to a given concentration is similar to the preparation of a polymer solution. We first prepared a high-concentration stock solution and then diluted it to a very low desired concentration. In all experiments, the rhodamine 6G concentration in the reservoir was set to 80 ppb.

A 540 nm short-pass optical filter was placed in front of the PIV camera (Phantom VEO340L), allowing the Mie scattering light to pass and rejecting the fluorescent light. For the LIF camera (Phantom V711), a 540 nm long-pass optical filter was used to capture only the fluorescent light. The two cameras were arranged along the same side of the laser sheet and a semi-transparent-semi-reflective mirror was used to split the light into two parts (figure 1*a*). Calibration was performed using the same calibration target (LaVision) for both the PIV and LIF measurements. In figure 1(*b,c*), we show the image of the fluorescence field and the image of seeding particles. The field of view (FOV) of the LIF camera is 66 mm × 105 mm in the streamwise and radial directions respectively, and is centred around the jet axis. The PIV only measures the upper half of the jet thanks to the fact that the jet is axisymmetric, the FOV of the PIV camera is 38 mm × 61 mm, and its size and position relative to the FOV of the LIF is shown by a rectangle in figure 1(*c*). The two cameras and the laser were synchronised such that the velocity and scalar fields could be simultaneously measured. The specific parameters of PIV and LIF are listed in table 1. The velocity and scalar concentration fields were recorded at a sampling rate of 400 Hz, with a time interval of 2.5 ms between adjacent velocity/scalar concentration fields, which is smaller than the Kolmogorov time scale in all our measurements, indicating that our PIV/LIF measurement is time-resolved. Both cameras are operated in double-frame mode and we used the first frame of the LIF image to calculate the scalar concentration. Each PIV/LIF measurement comprised 3000 image pairs, resulting in 3000 time-resolved instantaneous velocity and concentration fields. Six independent measurements were performed under the same experimental condition, yielding a total of 18 000 velocity and concentration fields, which are sufficient for the subsequent analysis. The acquired tracer particle image pairs were processed by a recursive iterative interrogation scheme (LaVision, DaVis 8.4.0). The initial correlations were performed with a 48 × 48 pixel interrogation window, followed by a 24 × 24 pixel window, and with a 75 % overlap in each interrogation step. The instantaneous velocity map contains 264 × 423 $(x{-}r)$ vectors, with a vector spacing of 0.143 mm. The spurious velocity vectors was less than 1 %, which was detected by a 5 × 5 median test and then



https://doi.org/10.1017/jfm.2025.231 Published online by Cambridge University Press

replaced by linear interpolation around neighbour vectors. The accuracy of the particle displacement was estimated to be around 0.1 pixel.

To relate the light intensity with the actual concentration of the scalar, a pixel-by-pixel calibration was performed. First, the background intensity $\overline{I_{bg}}(x, r)$ was obtained by averaging 1000 snapshots taken when no dye is added to the tank, where the bar denotes the time average. Then, the tank was filled with a well-mixed and known concentration (smaller than 80 ppb) rhodamine 6G solution. We captured 1000 snapshots to calculate the average intensity of the fluorescence, $\overline{I_{cal}}(x, r)$. This process was repeated six times using six different concentrations of rhodamine 6G solutions. The background subtracted average light intensity $\overline{I_{cal}}(x, r) - \overline{I_{bg}}(x, r)$ should depend linearly on the scalar concentration. Finally, the instantaneous scalar concentration $\phi_R(x, r)$ (the subscript $_R$ denotes rhodamine 6G) can be obtained using the following relation:

$$\frac{\phi_R(x, r)}{\phi_{R,cal}(x, r)} = \frac{\overline{I_{samp}}(x, r) - \overline{I_{bg}}(x, r)}{\overline{I_{cal}}(x, r) - \overline{I_{bg}}(x, r)}. \tag{2.1}$$

For accurate scalar concentration measurement, the laser intensity was kept the same during calibration and experiments.

Several factors, including light attenuation, secondary fluorescence effects and luminous efficiency, can affect the accuracy of the LIF (Baj *et al.* 2016). However, in our experiment, we employed fluorescent dye at extremely low concentrations (linear region) and the above-mentioned effects are negligible (Parker *et al.* 2020). Nevertheless, noise introduced by issues like laser intensity variation during the measurement can affect the final concentration field. To mitigate this noise, we applied a $3 \times 3$ pixel median filter to smooth the measured concentration field. The scalar concentration has a single-pixel resolution (around $0.6-1.4\eta$), and the spatial resolution of the velocity measurement is around $3-7\eta$. In the above, $\eta$ is estimated at the jet centreline for all the streamwise locations we measured in this study. The spatial resolution of our LIF measurement is sufficient to resolve the TNTI (Westerweel *et al.* 2009; Mistry *et al.* 2016; Kohan & Gaskin 2020).

Figure 2 shows typical examples of the instantaneous scalar concentration and velocity vector fields measured in the far field ($45 < x/D < 67$) of a pure water jet and two polymer-laden jets. The scalar concentration field provides a clear visualisation of the vortices generated by the flow. It is evident that turbulent mixing is significantly suppressed with polymer additives, resulting in more unmixed low-concentration and high-concentration fluid clumps concentrated near the centreline in the polymer-laden jet. Compared with the pure water case, high-concentration passive scalar can even be observed near the turbulent/non-turbulent boundary in the polymer-laden jet. It is also observed that the scalar field and vortices are elongated along the streamwise direction (Guimarães *et al.* 2020; Peng *et al.* 2023). The velocity field appears smoother with polymer additives, in line with previous observation that polymers suppress small-scale fluctuations (Zhang & Xi 2022).

To reveal the effects of polymers on the multi-scale nature of turbulence, we also measured the turbulent kinetic energy spectra. The resolution of the PIV camera (Phantom, VEO340L) was deliberately reduced to $144 \times 800$ pixels, thereby enabling a much higher sample rate of 2000 Hz, approximately 10 times faster than the smallest time scale at $x/D = 56$. The captured image pairs were processed using the same method outlined before, yielding a thin slab of velocity field in the radial direction. Each measurement, lasting 80 seconds, was repeated 7 times. For each measurement, a time series was constructed from the measured velocity field at a fixed location and a direct Fourier transformation was subsequently applied. As we have seven segments of velocity



https://doi.org/10.1017/jfm.2025.231 Published online by Cambridge University Press

https://doi.org/10.1017/jfm.2025.231 Published online by Cambridge University Press

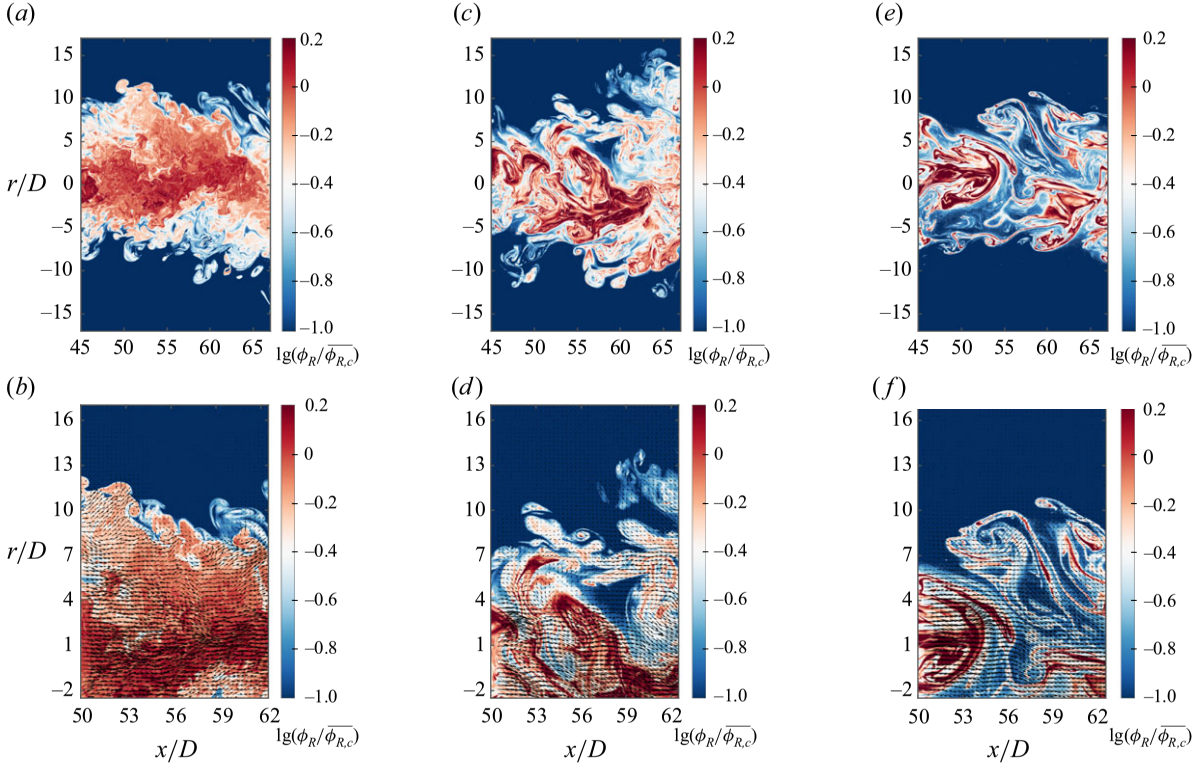



Figure 2. (*a*) Instantaneous concentration field, normalised by the averaged centreline scalar concentration $\overline{\phi_{R,c}}$ and shown in logarithmic scale, in the pure water jet at $Re = 7075$. (*b*) Velocity field is superimposed on the concentration field and the arrow length represents the magnitude of velocity. (*c,d*) and (*e,f*) Same as panels (*a*) and (*b*) but for $Wi = 36.7$ and 85.6, respectively.

| | Pure water | Entrainment transition | | Entrainment enhancement | |
|---|---|---|---|---|---|
| $\phi$[ppm] | — | 20 | 20 | 20 | 20 |
| $M_w$ [g mol$^{-1}$] | — | $5 \times 10^6$ | $8 \times 10^6$ | $4 \times 10^6$ | $5 \times 10^6$ |
| $\tau_p$ [ms] | — | 23.36 | 54.43 | 15.63 | 23.36 |
| $Wi$ | — | 36.7 | 85.6 | 24.6 | 36.7 |
| FOV of PIV ($x/D$) | [50, 62] | [35, 47] | [50, 62] | [35, 47] | [50, 62] |
| FOV of LIF ($x/D$) | [45, 67] | [30, 52] | [45, 67] | [30, 52] | [45, 67] |
| $R_b$ | 0.088 | 0.095 | 0.094 | 0.117 | 0.117 |
| $R_{b_\phi}$ | 0.115 | 0.128 | 0.129 | 0.159 | 0.157 |

Table 2. PIV and LIF measurement details. $\phi$, $M_w$, $\tau_p$ and $Wi$ denote the polymer concentration, molecular weight of the PEO, relaxation time of the PEO and Weissenberg number, respectively. The positions for the PIV and LIF measurements are also specified. Here $R_b$ and $R_{b_\phi}$ are the spreading rates of the velocity and scalar fields, respectively.

measurements, the final velocity power spectrum is obtained by averaging the seven power spectra from those seven velocity segments. The high-frequency noise plateau of the power spectra from the PIV measurement was corrected using the method proposed by Oxlade *et al.* (2012).

### 2.3. *Experimental parameters*

In our previous study (Peng *et al.* 2023), we used full-field PIV measurements to clearly demonstrate that polymer-laden jet evolves from the entrainment reduction regime near the jet exit to the entrainment enhancement regime further downstream, compared with the pure water case. We also found that the properties of the polymer-laden jet has very strong dependence on the Weissenberg number $Wi$ (Peng *et al.* 2023). Therefore, in this study, we performed four sets of PIV and LIF measurements with different $Wi$ and downstream locations, but at a fixed Reynolds number $Re = 7075$ and concentration $\phi = 20$ ppm (parts per million by weight) (see table 2). The $Wi$ was varied by using different molecular weights $M_w$ of PEO, and these ranged from 24.6 to 85.6. For the polymer solutions used here, the viscosity is practically the same as that of the solvent and the shear thinning effect is negligible (see Appendix A).

The instantaneous velocity $U_i(x, r)$ $(i = x, r)$ can be decomposed into time-averaged $\overline{U_i}(x, r)$ and fluctuation $u_i(x, r)$ components, i.e. $U_x(x, r) = \overline{U_x}(x, r) + u_x(x, r)$. Similarly, the scalar concentration $\phi_R$ is decomposed into the time-averaged part $\overline{\phi_R}$ and the fluctuating part $\phi_R'$. The effects of polymer additives at different $Wi$ on the mean and fluctuation velocity and scalar fields are discussed in Appendix B. The spreading rate is the slope of the jet half-width. It is necessary to mention that the $Wi = 24.6$ case at $x/D = [35, 47]$ and the $Wi = 36.7$ case at $x/D = [50, 62]$ are in the entrainment enhancement regime, where the spreading rate is approximately 33 % larger than that of the pure water case; while the $Wi = 36.7$ case at $x/D = [35, 47]$ and the $Wi = 85.6$ case at $x/D = [50, 62]$ are in a transition regime, where the spreading rate is slightly larger than that of the pure water case; see table 2. The entrainment reduction regime is not investigated here since the measured TNTI through LIF measurement is discontinuous in the central plane due to the out-of-plane motion of the jet most of the time. This regime has been investigated in great detail by direct numerical simulation (DNS) by Abreu *et al.* (2022).



https://doi.org/10.1017/jfm.2025.231 Published online by Cambridge University Press

| | Pure water | Entrainment transition | | Entrainment enhancement | |
|---|---|---|---|---|---|
| $Wi$ | — | 36.7 | 85.6 | 24.6 | 36.7 |
| $x/D$ | 56 | 41 | 56 | 41 | 56 |
| $Re_\lambda$ | 145 | 389 | 369 | 249 | 321 |
| $\lambda$ [mm] | 1.94 | 2.97 | 3.87 | 2.14 | 3.39 |
| $\eta$ [mm] | 0.082 | 0.077 | 0.10 | 0.069 | 0.096 |
| $\eta_B$ [mm] | 0.0014 | 0.0013 | 0.0017 | 0.0012 | 0.0016 |
| $\tau_\eta$ [ms] | 7.1 | 6.2 | 10.1 | 5.0 | 9.7 |
| $u_\eta$ [m s$^{-1}$] | 0.012 | 0.012 | 0.0093 | 0.014 | 0.0099 |
| $\varepsilon_d$ [m$^2$ s$^{-3}$] | 0.019 | 0.025 | 0.0078 | 0.038 | 0.010 |
| $\varepsilon_d b/U_c^3$ | 0.0099 | 0.0048 | 0.0024 | 0.0074 | 0.0059 |
| $Wi_{local}$ | — | 3.77 | 5.39 | 3.12 | 2.41 |

Table 3. Experimental parameters. $\phi$, $M_w$, $\tau_p$ and $Wi$ denote the polymer concentration, molecular weight of the PEO, relaxation time of the PEO and Weissenberg number, respectively. The positions for the PIV and LIF measurements are also specified. Here $R_b$ and $R_{b_\phi}$ are the spreading rates of the velocity and scalar fields, respectively.

The average kinetic energy dissipation rate $\varepsilon_d$ is calculated from the velocity gradient tensor under the axisymmetric hypothesis (Xu & Chen 2013), which is expressed as

$$\varepsilon_{d,axi} = \nu 8\overline{g_{rr}^2 - g_{xx}^2 + 2g_{xr}^2 + 2g_{rx}^2}, \tag{2.2}$$

where $\boldsymbol{g}_{ij}$ is the velocity gradient tensor. Due to the filtering effect of PIV algorithm, the measured $\varepsilon_d$ would be smaller than the 'true' dissipation rate (Lavoie *et al.* 2007). Since the filtering effect produces systematic error in both the Newtonian and the polymer-laden cases, we do not need to consider the filtering effect in our comparative study of the Newtonian and the polymer-laden jets. In addition, the measured $\varepsilon_d$ is non-zero in the non-turbulent region due to the measurement noise. This noise is Gaussian in nature and can be subtracted from the measured $\varepsilon_d$ (Westerweel *et al.* 2009). The $\varepsilon_d$ for all cases are listed in table 3.

The basic flow parameters, including the Kolmogorov length scale $\eta = (\nu^3/\varepsilon_d)^{1/4}$, Batchelor scale $\eta_B = \eta/\sqrt{Sc}$, Kolmogorov time scale $\tau_\eta = (\nu/\varepsilon_d)^{1/2}$, Kolmogorov velocity scale $u_\eta = (\nu\varepsilon_d)^{1/4}$, Taylor micro length scale and Taylor-scale-based Reynolds number $Re_\lambda = u_{rms}\lambda/\nu$, are listed in table 3, where $u_{rms} = \sqrt{(u_{x,rms}^2 + 2u_{r,rms}^2)/3}$ is the turbulent velocity fluctuation. Comparing the pure water case with the $Wi = 36.7$ and 85.6 cases at $x/D = 56$ (see table 3), it is clear that the kinetic energy dissipated by the fluid is suppressed, while the length scales ($\eta$ and $\lambda$) and Reynolds number are larger. The above observations are consistent with the results reported in planar jet (Guimarães *et al.* 2020) and isotropic turbulence (Rosti *et al.* 2023).

### 2.4. *Detection of the TNTI and determination of the entrainment velocity*

The isosurface of passive scalar is extensively employed in detecting TNTI in Newtonian jets (Westerweel *et al.* 2009; Mistry *et al.* 2016; Kohan & Gaskin 2020). The same method is employed here. We first determine the concentration threshold to discriminate the turbulent/non-turbulent regions. The details can be found in Appendix C.1. In this study, the concentration threshold $\phi_R/\phi_{R,c} = 0.18$, where $\phi_{R,c}$ is the concentration at the centreline. Once the TNTI is determined, a local coordinate system along the TNTI can be established (see the inset of figure 3*a*). Please note that $s_n < 0$ and $s_n > 0$ correspond to



https://doi.org/10.1017/jfm.2025.231 Published online by Cambridge University Press

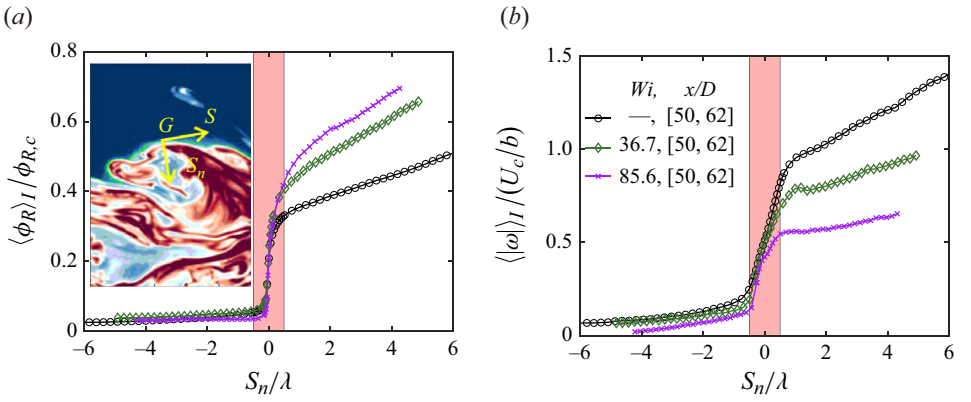



Figure 3. Conditionally averaged profiles of (*a*) scalar concentration, $\langle\phi_R\rangle_I/\phi_{R,c}$, and (*b*) out-of-plane vorticity magnitude, $\langle|\omega|\rangle_I/(U_c/b)$, along the local coordinate system, depicted as yellow arrows in the inset of panel (*a*). The rectangles, centred around $s_n = 0$, span a width of one Taylor length scale $\lambda$.

the non-turbulent and turbulent regions, respectively. Here, $\phi_R$ and out-of-plane vorticity $\omega$ can be further averaged condition on this local coordinate, which are denoted as $\langle\phi_R\rangle_I$ and $\langle\omega\rangle_I$. Interestingly, $\langle\phi_R\rangle_I/\phi_{R,c}$ and $\langle|\omega|\rangle_I/(U_c/b)$ exhibit a sharp increase across the TNTI as shown in figure 3, demonstrating that the scalar can be used to detect the TNTI in the presence of polymers.

The local entrainment velocity along the TNTI is measured by the interface tracking method proposed by Wolf *et al.* (2012). The displacement velocity of TNTI, $\boldsymbol{u_s}$, has two contributions: the local fluid flow advection, $\boldsymbol{u_I}$, and local entrainment across the TNTI, $v_n$. Consequently, $v_n\boldsymbol{s_n} = \boldsymbol{u_s} - \boldsymbol{u_I}$. The same method can be applied to a filtered scalar and velocity fields to calculate the local entrainment velocity at scale $\Delta$. More details on the determination of $v_n$ can be found in Appendix C.2.

## 3. Turbulence characteristics in polymer-laden jet

Turbulent flow and entrainment process are multi-scale in nature. It is found that polymers redistribute energy among different scales (Valente *et al.* 2014; Zhang *et al.* 2021). The degree of polymer extension and, in turn, its back-reaction on the flow depend on the local Weissenberg number (Guimarães *et al.* 2020, 2022). Figure 4(*a*) shows the radial profiles of $Wi_{local} = \tau_p/\tau_\eta$ at $x/D = 56$. Here, $Wi_{local}$ gradually decays along the radial direction as can be expected. At a fixed $x$, the interface is not immobile but fluctuates in the radial direction, so it will probe a different region of the flow. Thus, it is more instructive to calculate $Wi_{local}$ conditioned on the local coordinate system along the TNTI, $\langle Wi_{local}\rangle_I$, and this is shown in figure 4(*b*). The $\langle Wi_{local}\rangle_I$ is nearly 0 in the non-turbulent region ($s_n < 0$), experiences a sharp increase within the interface and then mildly increases in the turbulent region ($s_n > 0$). The $\langle Wi_{local}\rangle_I$ for the $Wi = 36.7$ and 85.6 cases is larger than 1 within the interface and in the turbulent region, where the local flow would be modified by polymers.

We compare the power spectra of turbulent velocity for pure water and polymer-laden jets at the same downstream location, as depicted in figure 5. At the centreline of a pure water jet, an inertial range with $-5/3$ scaling in the range of $10 < f < 10^2$ Hz is observed (figure 5*a*). In the dissipation range ($f > 10^2$ Hz), there is a rapid decay in energy content. With the addition of polymers, the $E(f)$ of $Wi = 36.7$ pivots at a frequency $f_p \approx 35$ Hz. Above this frequency, the energy content of the small-scales (high frequency) motion



https://doi.org/10.1017/jfm.2025.231 Published online by Cambridge University Press

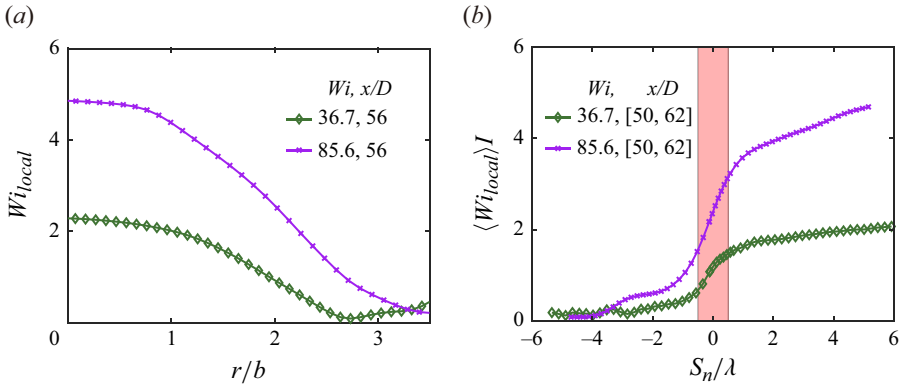



Figure 4. (*a*) Radial profiles of the local Weissenberg number, $Wi_{local}$, as a function of $r/b$ at streamwise position $x/D = 56$. (*b*) Conditionally averaged local Weissenberg number on the TNTI, $\langle Wi_{local}\rangle_I$, as a function of the distance $s_n$ from the TNTI. The vertical bar in panel (*b*) has a width of $\lambda$.

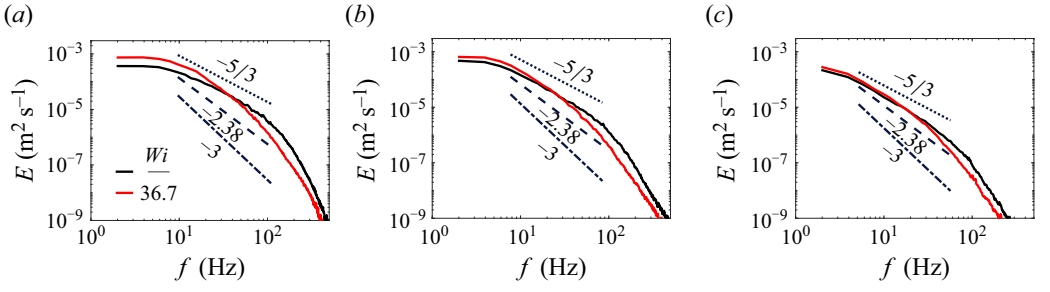



Figure 5. Power spectra of turbulent velocity at (*a*) $(x/D, r/b) = (56, 0)$, (*b*) $(x/D, r/b) = (56, 0.5)$ and (*c*) $(x/D, r/b) = (56, 1)$ for the pure water and $Wi = 36.7$ cases. $-5/3$ denotes the inertial range scaling in Newtonian turbulence. $-2.38$ and $-3$ are scaling exponents reported in inertio-elastic turbulence.

is suppressed; while below $f_p$, the energy content is augmented. The enhancement of large scales (low frequency) and suppression of small-scales motion aligns with previous findings in Rayleigh–Taylor turbulence (Boffetta *et al.* 2011).

In figure 5(*a*), we also show two reference slopes frequently reported in the literature: $-2.38$ and $-3$. Zhang *et al.* (2021) reported an exponent of $-2.38$ in von Kármán flow, which was later confirmed in numerical simulation (Rosti *et al.* 2023). In viscoelastic Taylor–Couette flow, Moazzen *et al.* (2023) reported a decay exponent of $-2.3$ extracted from the spatiotemporal maps obtained by flow visualisation; Boulafentis *et al.* (2024) found that the scaling exponent is close to $-2.5$. Valente *et al.* (2016) investigated a wide range of $Wi$ and found that the exponent first decreases from $-5/3$ to $-3$ and then increases back to $-5/3$ as $Wi$ grows. Other studies also pointed towards an exponent of $-3$ (Vonlanthen & Monkewitz 2013; Yamani *et al.* 2021; Guimarães *et al.* 2022; Soligo & Rosti 2023). It seems that the scaling exponent depends on $Re$ and $Wi$, and even the flow investigated. Due to the relatively low $Re$ here, the scaling range spans less than one frequency decade, it is hard to determine the scaling exponent. However, faster decay of the spectra in the inertial range is consistently observed, implying that the nonlinear energy transfer of the fluid is depressed.

Moving from $r/b = 0$ to $r/b = 0.5$ (figure 5*b*), a similar effect on small scales is observed. The energy content of large scales only slightly increases, not as dramatically as that at $r/b = 0$. Further away from the centreline ($r/b = 1$, figure 5*c*), the velocity becomes



https://doi.org/10.1017/jfm.2025.231 Published online by Cambridge University Press

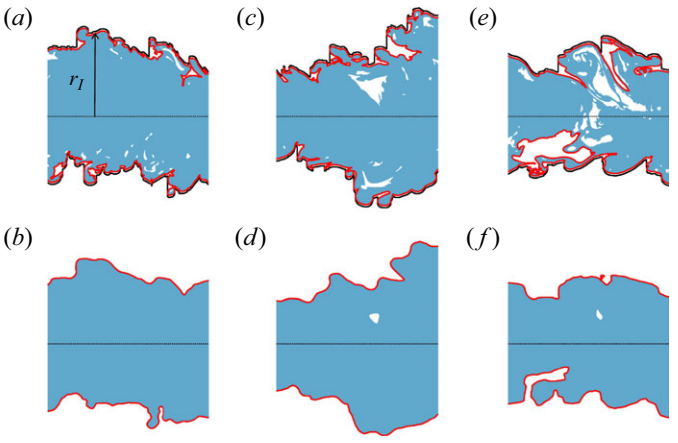



Figure 6. TNTI at multi-scales. The binarised images of the filtered scalar field, with filter sizes of (*a,c,e*) $\Delta/\eta \approx 3$ and (*b,d,f*) $\Delta/\eta \approx 80$, correspond to the cases of (*a,b*) pure water, (*c,d*) $Wi = 36.7$ and (*e,f*) $Wi = 85.6$. The red lines represent the TNTI and the black lines are the interface envelope. The interface envelope is shifted by 0.3 mm in the radial direction to distinguish it from the TNTI. The dotted lines are the jet centreline.

more intermittent due to the presence of non-turbulent regions, as will be discussed in figure 7. A slight deviation from the $-5/3$ scaling in the Newtonian case is observed in figure 5(*c*), which may result from the small $Re_\lambda$ in this radial position. It can be concluded that while the dissipative scale motions are consistently depressed in the radial direction, the effect of polymers on the inertial and energy-containing ranges of the kinetic energy spectrum strongly depend on the local Weissenberg number $Wi_{local}$. At the energy containing range of the spectrum, the turbulent energy is increased by the polymers.

## 4. Local entrainment along the turbulent/non-turbulent interface

As reported in our previous study (Peng *et al.* 2023), the polymer additives suppress entrainment in the near field of the jet. The entrainment reduction phenomenon was thoroughly investigated by Abreu *et al.* (2022) and attributed to a smoother TNTI in the viscoelastic case. However, in the far field of a viscoelastic jet, the entrainment rate significantly increases. This section delves into the underlying mechanism in the entrainment transition and enhancement regimes.

### 4.1. *Engulfment flux*

Engulfment is the process that the non-turbulent ambient fluid is transported into the turbulent core region by the large-scale inviscid motion (Roshko 1976; Westerweel *et al.* 2009; Jahanbakhshi & Madnia 2016; Long *et al.* 2022). Figure 6 shows the binarised images of instantaneous scalar concentration snapshots at the threshold of $\phi_R/\phi_{R,c} = 0.18$. The red lines depict the TNTI on both sides of the jet. The white clumps within the interfaces are unmixed fluids that are drawn from the non-turbulent region by the engulfment process and are named as bubbles (Westerweel *et al.* 2009; Long *et al.* 2022; Xu *et al.* 2023). As $Wi$ increases, more bubbles are engulfed into the turbulent region and the TNTI exhibits significant fluctuation in the radial direction.

The radial position of TNTI relative to the centreline is defined as $r_I$, as shown in figure 6(*a*). Figure 7 shows the probability density functions (p.d.f.s) of $r_I$ at $x/D = 56$, but with two filter sizes $\Delta/\eta \approx 3$ and 80. In our measurement, we will get two interfaces as depicted in figure 6: a top and bottom one with respect to the jet centreline.



https://doi.org/10.1017/jfm.2025.231 Published online by Cambridge University Press

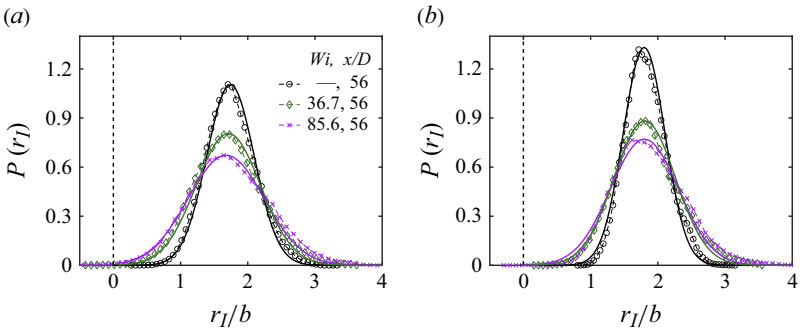



Figure 7. P.d.f.s of the radial position $r_I$ (normalised by the half-width $b$) of the TNTI with different filter size: (*a*) $\Delta/\eta \approx 3$ and (*b*) $\Delta/\eta \approx 80$. The solid lines represent Gaussian distribution.

The p.d.f.s shown in figure 7 use $r_I$ of the top interface, and a similar result will be obtained when using the bottom one since the jet is axisymmetric. The p.d.f. of $r_I$ for the pure water jet approximately follows a Gaussian distribution as observed by Kohan & Gaskin (2020), Westerweel *et al.* (2009) and Mistry *et al.* (2019). In addition, the p.d.f. is negatively skewed, which is associated with the engulfment process (Long *et al.* 2022). Figure 7(*a*) also shows that the p.d.f. of $r_I$ is still approximately Gaussian in a polymer-laden jet, with the maximum probability happening at the same radial position as the Newtonian case when $r_I$ is normalised by the jet half-width $b$. Please note that the p.d.f.s of $r_I$ at different $x$ collapse onto a master curve when $r_I$ is normalised by $b$ in the Newtonian case (Mistry *et al.* 2016). For the polymer-laden jet, the p.d.f. of $r_I$ is wider on the both sides of the tail, signalling stronger large-scale fluctuation of TNTI in the polymer-laden jet. There are even some events with $r_I < 0$ at high $Wi$ in figure 7, meaning that both interfaces are located on the same side relative to the jet centreline, i.e. $r_I < 0$ for both interfaces. This phenomenon, however, is rarely observed in a Newtonian jet. At a larger filter size (figure 7*b*), observations similar to those in figure 7(*a*) are noted. The above result indicates that large scale motions play an important role on increasing the motion of TNTI.

The centroid and area $S$ of the bubbles within TNTI can be readily estimated from figure 6(*a,c,e*), with $\sqrt{S}$ being taken as the characteristic size of the bubble. The p.d.f.s of bubble centroid radial position $r_{bub}$ and bubble size $\sqrt{S}$ are shown in figure 8. As $Wi$ increases, more bubbles appear near the jet centreline, corroborating the direct observations in figure 6(*a,c,e*). In the Newtonian case, bubbles are predominantly near the TNTI, with rare occurrences of bubbles at the centre (Xu *et al.* 2023). However, in the $Wi = 85.6$ case, we can frequently observe bubbles in the centre. This phenomenon can be attributed to two processes. On one hand, polymers enhance the large scale motion, which results in higher radial position fluctuation of TNTI as shown in figure 7. When the TNTI is close to the centreline, the ambient non-turbulent fluid is more likely to be engulfed into the centre. On the other hand, polymers suppress the small scales, which reduces small-scale mixing. In that way, a bubble can persist for a longer time and be advected to the centre before being digested by the turbulent motion in the core region. Similarly, in figure 9, we also present the p.d.f.s of scalar concentration $\phi_R/\phi_{R,c}$ sampled on the turbulent core region. The probabilities of both low and high concentrations increase with $Wi$, as indicated by the larger standard deviation (std) of $\phi_R/\phi_{R,c}$. The coexistence of low and high scalar concentrations within the turbulent core region suggests that the small-scale mixing is hindered by polymers, aligning with the measured power spectra of



https://doi.org/10.1017/jfm.2025.231 Published online by Cambridge University Press

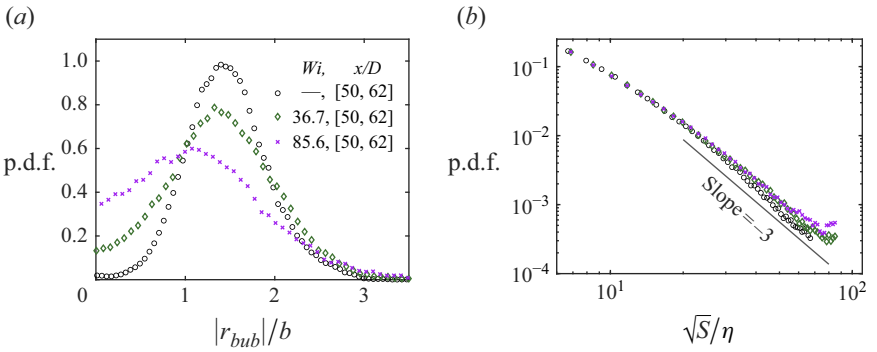



Figure 8. (*a*) P.d.f.s of the radial position of the bubble centroid. (*b*) P.d.f.s of the bubble size within the turbulent region.

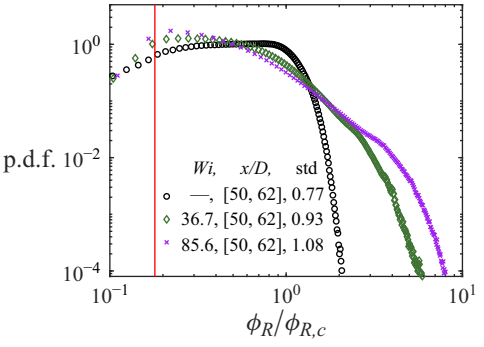



Figure 9. P.d.f.s of the scalar concentration $\phi_R/\phi_{R,c}$, sampled within the TNTI. The standard deviations of $\phi_R/\phi_{R,c}$ are also indicated in the legend. The vertical red line represents the scalar concentration threshold $\phi_R/\phi_{R,c} = 0.18$ used in this study.

turbulent velocity. It should be noted that scalars with $\phi_R/\phi_{R,c} < 0.18$ are located inside the bubbles. The larger probability of $\phi_R/\phi_{R,c} < 0.18$ also signifies more bubbles in the turbulent core region. The p.d.f.s of the bubble size are depicted in figure 8(*b*), where the p.d.f.s nearly overlap. The bubble size follows a power-law distribution with an exponent of $-3$, a scaling close to that reported in the distribution of the size of the irrotational fluid region within the turbulent core (da Silva *et al.* 2014*b*).

In the viscoelastic jet, more bubbles are engulfed into the turbulent region. One may wonder whether polymers have some effects on these bubbles or not. Figure 10 presents the mean streamwise velocity and out-of-plane vorticity within the bubbles, normalised by $U_c$ and $U_c/b$, respectively, i.e. $\overline{U_{x,bub}}/U_c$ and $\overline{|\omega|_{bub}}/(U_c/b)$. For the mean streamwise velocity, we find that $\overline{U_{x,bub}}/U_c$ exhibits a similar trend and magnitude with the mean streamwise velocity $\overline{U_x}/U_c$. However, the out-of-plane vorticity, $\overline{|\omega|_{bub}}/(U_c/b)$, remains nearly constant within error bars in the radial direction. These observations suggest that while bubbles have gained momentum from the background turbulence, they have not mixed with the surrounding fluid to acquire more vorticity, indicating that engulfment is an inviscid process. Polymers augment the large-scale inviscid motion of turbulence, resulting in more bubbles being engulfed into the turbulent region. It is also interesting to note that $\overline{|\omega|_{bub}}/(U_c/b)$ in the viscoelastic case seems to be suppressed compared with the Newtonian case, though there are large error bars of the data. This behaviour indicates that



https://doi.org/10.1017/jfm.2025.231 Published online by Cambridge University Press

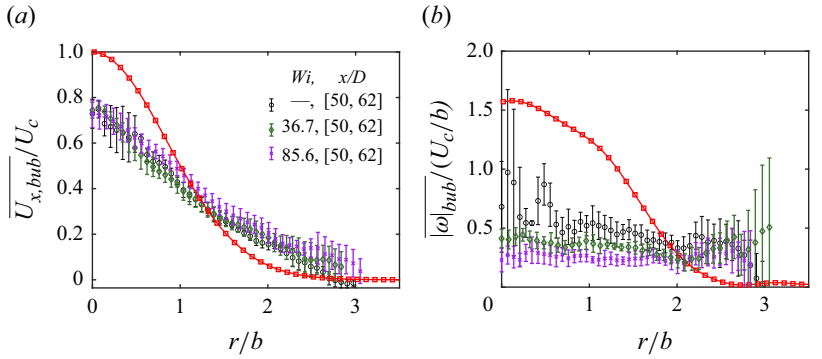



Figure 10. Radial profiles of (*a*) the normalised streamwise velocity $\overline{U_{x,bub}}/U_c$ and (*b*) the normalised out-of-plane vorticity $\overline{|\omega|_{bub}}/(U_c/b)$ in the bubbles. For comparison, the mean streamwise velocity $\overline{Ux}/U_c$ and out-of-plane vorticity $\overline{|\omega|}/(U_c/b)$ from the pure water case are also depicted, represented by red squares. The error bars in panel (*a,b*) denote one standard deviation. The large error bars of $\overline{|\omega|_{bub}}/(U_c/b)$ near $r/b \approx 0$ and $r/b \approx 3$ result from the limited data at these radial positions.

when bubbles get across the TNTI, they acquire less vorticity in the presence of polymer, which may be related to the depression of vorticity production or diffusion by polymers (Cai *et al.* 2010; Guimarães *et al.* 2022).

The observed phenomena suggest that polymer additives enhance the engulfment process due to the augmented large-scale inviscid motion. It is essential to determine the fraction of the total entrainment flux contributed by the engulfment flux. Westerweel *et al.* (2009) proposed that all unmixed low-concentration fluids within the TNTI envelope, formed by the junction of the outermost part of TNTI (refer to the black lines in figure 6*a,c,e*), result from engulfment. The total mass flux, denoted as $Q$, is expressed as

$$Q = 2\pi\rho \int_0^\infty \overline{U_x(r)} r \, \mathrm{d}r = 2\pi\rho U_c b^2 \int_0^\infty \xi f(\xi) \mathrm{d}\xi, \tag{4.1}$$

where $U_c$ is the mean streamwise velocity at the centreline, $\xi = r/b$ is the scaled radial position and $f(\xi) = \overline{U_x}(\xi)/U_c$ is the scaled mean streamwise velocity. The entrainment rate $\mathrm{d}Q/\mathrm{d}x$ is the slope of total mass flux, i.e.

$$\frac{\mathrm{d}Q}{\mathrm{d}x} = 2\pi\rho(U_c b)\frac{\mathrm{d}b}{\mathrm{d}x}\int_0^\infty \xi f(\xi)\mathrm{d}\xi. \tag{4.2}$$

Here, $U_c b$ is constant along the streamwise direction since the momentum is conserved (Peng *et al.* 2023). Also, $f(\xi)$ is the same for both Newtonian and viscoelastic jets (see appendix B). Thus, $\mathrm{d}Q/\mathrm{d}x$ is proportional to $\mathrm{d}b/\mathrm{d}x$. For the interior of the TNTI envelope, the enclosed jet mass flux $Q_{jet}$ is defined as

$$Q_{jet} = 2\pi\rho \int_0^\infty \overline{U_x(r)} \mathrm{p}_{jet}(r) r \, \mathrm{d}r, \tag{4.3}$$

where $\mathrm{p}_{jet}(r)$ represents the probability that the jet is within the TNTI envelope at the radial position $r$. The contribution of engulfment can be estimated from the volume of the unmixed low-concentration fluids within the TNTI envelope. Consequently, the engulfment mass flux, $Q_{engulf}$, can be estimated by the equation,

$$Q_{engulf} = 2\pi\rho \int_0^\infty \overline{U_x(r)} \mathrm{p}_{engulf}(r) r \, \mathrm{d}r, \tag{4.4}$$



https://doi.org/10.1017/jfm.2025.231 Published online by Cambridge University Press

| | Pure water | Entrainment transition | | Entrainment enhancement | |
|---|---|---|---|---|---|
| $Wi$ | — | 36.7 | 85.6 | 24.6 | 36.7 |
| $x/D$ | 56 | 41 | 56 | 41 | 56 |
| $Q$[kg·s$^{-1}$] | 0.290 | 0.186 | 0.235 | 0.221 | 0.280 |
| d$Q$/d$x$ [kg·(m·s)$^{-1}$] | 1.81 | 2.08 | 2.05 | 2.41 | 2.42 |
| $Q_{jet}$ [kg·s$^{-1}$] | 0.246 | 0.144 | 0.168 | 0.183 | 0.220 |
| $Q_{engulf}$ [kg·s$^{-1}$] | 0.023 | 0.038 | 0.061 | 0.035 | 0.059 |
| $Q_{jet}/Q$ | 84.8 % | 77.4 % | 71.5 % | 82.8 % | 78.5 % |
| $Q_{engulf}/Q$ | 7.9 % | 20.4 % | 25.9 % | 15.8 % | 21.1 % |

Table 4. Mass flux in the pure water and polymer-laden jets. Here $Q$, $Q_{jet}$ and $Q_{engulf}$ denote the total mass flux, mass flux within the TNTI envelope and engulfment mass flux, respectively.

where $p_{engulf}(r)$ denotes the probability that the low scalar concentration fluid, with $\phi_R/\phi_{R,c} < 0.18$, is within the TNTI envelope at the radial position $r$. The mass fluxes $Q$, $Q_{jet}$ and $Q_{engulf}$ at specific $x/D$ are tabulated in table 4. The results indicate that the contribution of engulfment in pure water jet, $Q_{engulf}/Q$, is 7.9 %, in good agreement with previous study (Westerweel *et al.* 2009). This suggests that engulfment is not the primary mechanism in the entrainment process of a Newtonian jet, a conclusion also reported in studies on a synthetic jet and boundary layer (Long *et al.* 2022; Xu *et al.* 2023), where the entrainment flux due to engulfment does not exceed 10 %.

In the viscoelastic case, the contribution of engulfment to entrainment, $Q_{engulf}/Q$, increases with $Wi$. The maximum contribution is approximately 25.9 % in the $Wi = 85.6$ case. Despite the significant enhancement of the contribution due to engulfment compared with the Newtonian case, we conclude that engulfment is still not the primary mechanism in the entrainment of a polymer-laden jet over the parameter range investigated here. In the entrainment enhancement regime, the engulfment process is significantly increased, suggesting the importance of the engulfment process in enhancing the entrainment. It would be interesting to further increase $Wi$ to examine the role of engulfment in the entrainment of a polymer-laden jet. However, it should be noted that in experiments, polymer chains may degrade due to strong shear at higher $Wi$ values.

Considering the $Wi = 36.7$ case in the entrainment transition regime ($x/D = 41$) and entrainment enhancement regime ($x/D = 56$), although $Q$, $Q_{jet}$ and $Q_{engulf}$ all increase in the streamwise direction, the jet and engulfment contribution to the total flux remain relatively constant in the streamwise direction (refer to the third and sixth rows of table 4). This suggests that the engulfment process does not play a role in governing the change from the entrainment transition regime to the entrainment enhancement regime. It should be emphasised here that we use 'entrainment enhancement regime' to represent that in that regime, the entrainment rate is enhanced, not the entrainment itself (total mass flux). Actually, in the entrainment enhancement regime, the entrainment or the total mass flux $Q$ is reduced compared with that in the Newtonian jet (compare the fifth row with the second row of table 4). This is due to the fact that the entrainment is significantly reduced in the near field, which results in smaller $Q$. Further downstream, $Q$ in the viscoelastic jet exceeds that in the Newtonian jet as shown in our previous study (Peng *et al.* 2023).

### 4.2. *Entrainment flux along the turbulent/non-turbulent interface*

In § 4.1, we analyse the impact of polymer additives on the engulfment process, where the ambient quiescent fluid parcels are engulfed into the turbulent core region by the



https://doi.org/10.1017/jfm.2025.231 Published online by Cambridge University Press

large-scale inviscous eddies. However, recent studies showed that the entrainment is a multi-scale process along the TNTI (Meneveau & Sreenivasan 1990; Mistry *et al.* 2016), with the entrainment rate depending on the surface area $S$ and entrainment velocity $V_n$. At the smallest length scale (of order of $\eta$), $V_n$ is small but is balanced by a large $S$ since the surface is convoluted. While at large scales, $V_n$ is large but is balanced by a small $S$ since the surface is smooth. Hence, the entrainment rate, $S(\Delta)V_n(\Delta)$, estimated at different scale $\Delta$ is scale-invariant. In the inertial range of scales, the TNTI is multi-fractal, i.e. $S(\Delta) \sim \Delta^{-D_3}$ with the scaling exponent $2.3 < D_3 < 2.4$ (Mistry *et al.* 2016). Accordingly, $V_n(\Delta) \sim \Delta^{D_3}$ in the inertial range. In this section, we will delve into the effects of polymers on the those two contributing factors: $S(\Delta)$ and $V_n(\Delta)$.

In our experiment, two-dimensional velocity and scalar concentration fields are available, from which TNTI length $L_{TNTI}$ and local entrainment velocity $v_n$ projected on the $x-r$ plane can be estimated. Given the axisymmetric nature of the jet, the mean entrainment velocity is given by

$$V_n = \overline{\left[ \frac{\int_0^{L_{TNTI}} (-v_n) r_I \mathrm{d}s}{\int_0^{L_{TNTI}} r_I \mathrm{d}s} \right]}, \tag{4.5}$$

which is integrated on the local coordinate along the TNTI. From the two-dimensional measurement, $L_{TNTI}(\Delta) \sim \Delta^{2-D_3}$ and $V_n(\Delta) \sim \Delta^{D_3-2}$ in the Newtonian case.

In figure 11(*a,b*), we show $L_{TNTI}$ and $V_n$ of the pure water case. For the pure water case, $L_{TNTI}$ scales with the filter size $\Delta$ in the log-log plot between $\lambda$ and $b$ (we take $b$ as the integral length scale), i.e. $L_{TNTI} \sim \Delta^{2-D_3}$ with $D_3 \approx 2.31$. Here, $V_n$ increases with $\Delta$ and follows a power-law scaling in the inertial range with an exponent $D_3 - 2 \approx 0.31$. Those two scalings, $L_{TNTI} \sim \Delta^{-0.31}$ and $V_n \sim \Delta^{0.31}$, together make the entrainment rate, $L_{TNTI}(\Delta)V_n(\Delta)$, independent of scales, which was corroborated in experiment by Mistry *et al.* (2016). We also note that the scaling range of $V_n$ is shorter than that of $L_{TNTI}$, probably due to the small Reynolds number ($Re_\lambda = 106$ at $x/D = 56$) in our study.

We start our analysis with the $Wi = 36.7$ case in the entrainment transition regime at $x/D = [35, 47]$. The scaling exponent of $L_{TNTI}$ is altered by polymers, with a least-square fit yielding $2 - D_3 \approx -0.23$. The corresponding $D_3 \approx 2.23$, indicating that the interface is smoother than that of the pure water case at small scales, in line with the numerical simulation (Abreu *et al.* 2022). The scaling exponent of $V_n$ changes accordingly, i.e. $V_n \sim \Delta^{0.23}$, despite the short scaling range. The multi-scale nature of the entrainment velocity in the viscoelastic case has not been investigated in previous study. Previous studies showed that the small-scale end of the inertial range will be modified with the addition of polymers and a new scaling range will emerge between the inertial and dissipation ranges at high elasticity (Valente *et al.* 2016; Zhang *et al.* 2021). In turbulent jet flow, the scaling of the power spectrum of fluctuating velocity is altered, as has already been observed in figure 5(*a,b*). The change in the energy content among different scales will then modulate the scaling of $L_{TNTI}$ and $V_n$ in the polymer-laden jet.

At the small-length scale ($\Delta < \lambda$), the inertial force can be neglected and the viscous diffusion becomes dominated. Hence, the viscous nibbling is the dominating mechanism of entrainment at small scales. In the Newtonian jet, enstrophy production, viscous diffusion and viscous dissipation contribute to the nibbling process (Holzner & Lüthi 2011; Wolf *et al.* 2012; Watanabe *et al.* 2014; Abreu *et al.* 2022; Long *et al.* 2022). In viscoelastic fluid, Abreu *et al.* (2022) reported that vorticity diffusion induced by polymer elastic stress also contributes to the nibbling velocity. With the addition of polymers, the small-scale fluctuation is suppressed (Valente *et al.* 2016; Zhang *et al.* 2021; Zhang & Xi 2022) and the enstrophy production is also inhibited by polymers (Cai *et al.* 2010;



https://doi.org/10.1017/jfm.2025.231 Published online by Cambridge University Press

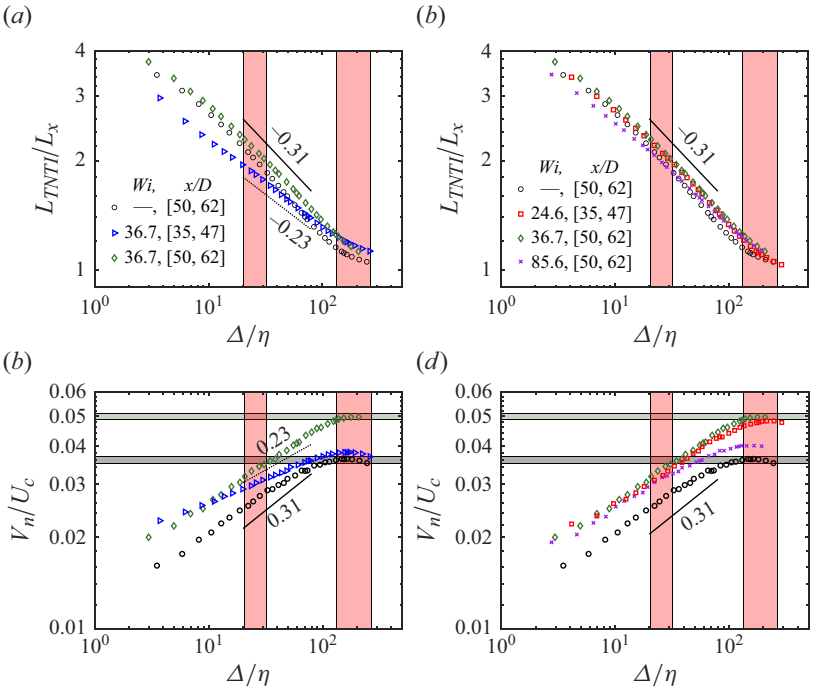



Figure 11. (*a,c*) TNTI length, $L_{TNTI}$ (normalised by $L_x$), and (*b,d*) mean entrainment velocity, $V_n$ (normalised by the mean centreline axial velocity $U_c$), as a function of the filter size $\Delta$. $L_x = 12D$ represents the length of the measurement region along the flow direction. The two vertical bars represent the Taylor scale $\lambda$ (left) and the integral scale $b$ (right) within the measurement range. The black horizontal bar denotes the large scale entrainment coefficient of the pure water case in the self-similar regime. The green horizontal bar denotes the large scale entrainment coefficient of the polymer-laden case in the entrainment enhancement regime.

ur Rehman *et al.* 2022). We would then expect that the contributions from enstrophy production, viscous diffusion and viscous dissipation are depressed accordingly, as was observed by Abreu *et al.* (2022). At the smallest scale we resolved here ($\Delta \approx 3\eta$), we find that $V_n$, however, is larger than that of the pure water case, implying that polymer elastic stress contributes to increase the entrainment velocity, i.e. elastic stress plays an important role in the local entrainment at small scales in the polymer-laden jet, in line with previous simulation (Abreu *et al.* 2022).

For the $Wi = 36.7$ case in the entrainment enhancement regime at $x/D = [50, 62]$, the scalings of $L_{TNTI}$ and $V_n$ are almost the same as those of the pure water case in figure 11(*a,b*). This observation seems contradictory with the enhanced $V_n$ and modified power spectrum in figure 5, all pointing to a different scaling of $L_{TNTI}$ and $V_n$. However, two important features need to be noted: (i) the radial position of TNTI is larger than $b$, i.e. $r_I > b$, most of the time; (ii) the flow becomes weaker along the radial direction as shown in figure 4. The whole range of scales including the scaling exponent are altered by polymers near the centre ($0 \leqslant r/b \leqslant 0.5$), while polymers primarily affect the dissipative scales when $r/b \geqslant 1$, and the scaling exponent remains nearly unaffected. The same scaling of $L_{TNTI}$ and $V_n$ for the $Wi = 35.6$ case at $x/D = [50, 62]$ can be understood from the fact that, in this downstream region and near the TNTI, polymers suppress the dissipative scale fluctuations but will not modify the scaling for scales between the dissipative and integral length scales.

Morton *et al.* (1956) proposed that $V_n$ is proportional to $U_c$, i.e. $V_n = \alpha U_c$ with $\alpha$ being the entrainment coefficient, and the entrainment rate is $b(x)\alpha U_c(x)$ at the large scale.



https://doi.org/10.1017/jfm.2025.231 Published online by Cambridge University Press

In our previous study, we have shown that $b(x)U_c(x)$ is constant in the streamwise direction and will not be changed by polymers (Peng *et al.* 2023). The entrainment rate thus merely depends on the $\alpha$. From figure 11(*b*), we find that $V_n$ increases with $\Delta$ and approaches a constant when $\Delta$ is close to $b$. The plateau, marked with a horizontal bar, gives the entrainment coefficient $\alpha$. For the Newtonian case, $\alpha = 0.036 \pm 0.001$ (black horizontal bar), in agreement with the value reported by Mistry *et al.* (2016). In the entrainment enhancement regime ($Wi = 36.7$ case at $x/D = [50, 62]$), $\alpha = 0.050 \pm 0.001$, which is increased by approximately 38 % compared with the Newtonian case. In the transition regime ($Wi = 36.7$ case at $x/D = [35, 47]$), $V_n/U_c$ at small scale is comparable to that at $x/D = [50, 62]$. However, due to the different scaling of $V_n$, $V_n$ at $x/D = [35, 47]$ gradually departs from that at $x/D = [50, 62]$ for $\lambda < \Delta < b$. Additionally, $\alpha$ at $x/D = [35, 47]$ is only slightly larger when compared with the Newtonian case.

Comparing $L_{TNTI}$ and $V_n$ in the entrainment transition and enhancement regimes at $Wi = 36.7$, we learn that polymers alter the scaling of $L_{TNTI}$ and $V_n$ in the entrainment transition regime, and the scaling remains the same in the entrainment enhancement regime. This may be related to a different degree of polymer elasticity. In the entrainment transition regime, the turbulence intensity is high enough to stretch polymers to a large degree, which in turn alter the scaling of $L_{TNTI}$ and $V_n$ (Xi *et al.* 2013; Valente *et al.* 2014; Zhang *et al.* 2021). In the entrainment enhancement regime, turbulence decays so that the polymers are stretched to a less degree, then the back reaction is not strong enough to alter the scaling of $L_{TNTI}$ and $V_n$ in the inertial range. Guimarães *et al.* (2024) recently showed the existence of different regimes of polymer conformation as the flow evolves downstream, e.g. the high-elasticity and low-elasticity regions. The entrainment transition and enhancement regimes thus may correspond to the high-elasticity and low-elasticity regions of polymer conformation reported in their study, respectively.

The $L_{TNTI}$ and $V_n$ from different Weissenberg number cases are shown in figure 11(*c,d*). We first compare $L_{TNTI}$ and $V_n$ from the $Wi = 24.6$ case at $x/D = [35, 47]$ and the $Wi = 36.7$ case at $x/D = [50, 62]$, which are both in the entrainment enhancement regime. It is found that $L_{TNTI}$ and $V_n$ from those two cases overlap with each other. Our results show that not only the global statistics, such as the normalised mean velocity and velocity fluctuation profiles, but also the local properties, including the TNTI length and entrainment velocity, are independent of the Weissenberg number, further demonstrating the universal nature in the entrainment enhancement regime. We then compare $L_{TNTI}$ and $V_n$ from the $Wi = 36.7$ and $Wi = 85.6$ cases at the same downstream region ($x/D = [50, 62]$). At $x/D = 56$, $Wi_{local}$ in the $0 \leqslant r/b < 2$ for the $Wi = 85.6$ case is larger than 2.2, which is the $Wi_{local}$ at the centreline for the $Wi = 36.7$ case (figure 4). Due to the larger $Wi_{local}$, we observe that the scaling exponents of $L_{TNTI}$ and $V_n$ for the $Wi = 85.6$ case are modified when compared with the $Wi = 36.7$ case. The corresponding scaling exponent $D_3 \approx 2.27$.

In the above, the enhanced $V_n$ at small scale is ascribed to the polymer elastic stress, as also reported in numerical simulation (Abreu *et al.* 2022). In a turbulent jet, the flow is inhomogeneous in the radial direction. Mistry *et al.* (2016) studied the conditionally averaged value of $v_n$ on $r_I$, denoted as $-\langle v_n \rangle|_{r_I}$. They found that the local entrainment is larger when TNTI is close to the centreline and $-\langle v_n \rangle|_{r_I}$ monotonically decreases with $r_I$. The local mean entrainment velocity at a specific $r_I$ also depends on the p.d.f. of $r_I$ ($P(r_I)$), namely $-\langle v_n \rangle|_{r_I} P(r_I)$. Integrating $-\langle v_n \rangle|_{r_I} P(r_I)$ in the radial direction yields the mean entrainment velocity. In figure 12, we compare $-\langle v_n \rangle|_{r_I} P(r_I)$ between the pure water jet and the polymer-laden one. Here, $-\langle v_n \rangle|_{r_I} P(r_I)$ for the polymer-laden jet is larger than that for the pure water one at the same $r_I$, presumably due to the polymer elastic stress. There is also another contribution that needs to be stressed. We have observed



https://doi.org/10.1017/jfm.2025.231 Published online by Cambridge University Press

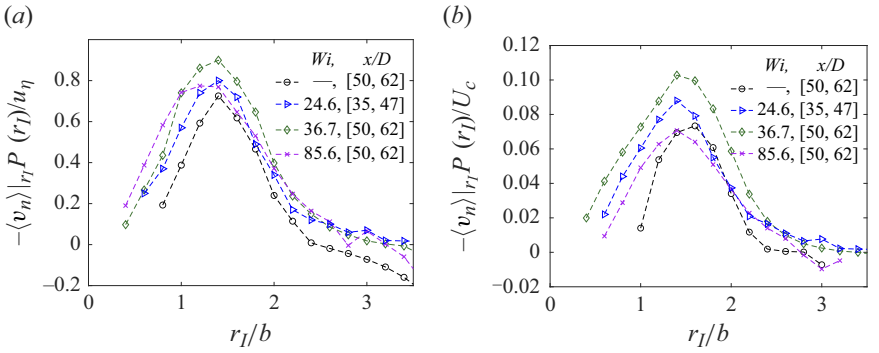



Figure 12. Entrainment velocity conditioned on the radial location of the TNTI $-\langle v_n\rangle|_{r_I} P(r_I)$ at two filter sizes (*a*) $\Delta/\eta \approx 3$ and (*b*) $\Delta/\eta \approx 80$.

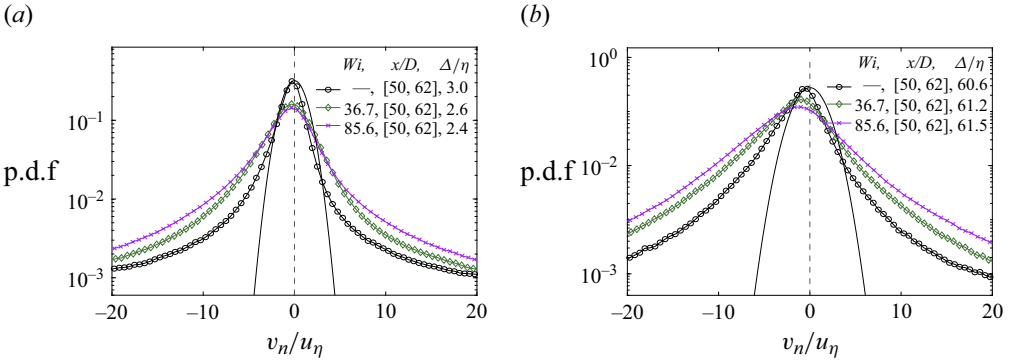



Figure 13. P.d.f.s of the local entrainment velocity $v_n$ at two filter sizes (*a*) $\Delta/\eta \approx 3$ and (*b*) $\Delta/\eta \approx 60$. The black curves represent Gaussian distribution.

that the tails of $P(r_I)$ becomes wider with the addition of polymers. The larger $-\langle v_n\rangle|_{r_I}$ and higher probability of $P(r_I)$ near the centreline will also contribute to the enhanced entrainment velocity; see the $-\langle v_n\rangle|_{r_I} P(r_I)$ curves within $0 < r_I/b < 1$ in figure 12.

Figure 13 depicts the p.d.f.s of the local entrainment velocity $v_n$ at both small ($\Delta/\eta \approx 3$) and large ($\Delta/\eta \approx 60$) scales. Please note that the mean entrainment velocity $V_n$ is of order of $u_\eta$. The local $v_n$ acquire values an order of magnitude larger than $u_\eta$, whose probability is much higher with respect to the Gaussian distribution (see the black lines in figure 13). The p.d.f.s are also negatively skewed, signifying the outward spreading tendency of the turbulent region (Holzner & Lüthi 2011; Wolf *et al.* 2012; Krug *et al.* 2015; Mistry *et al.* 2016; Long *et al.* 2022). In the polymer-laden jet, both tails of the p.d.f.s become wider, namely the local entrainment ($v_n < 0$) and detrainment ($v_n > 0$) velocity are both increased. Therefore, the behaviours of TNTI, including its radial position and velocity, are more intermittent in the viscoelastic jet as a result of the augmented large-scale motion.

## 5. Conclusions

We present an experimental study on the effects of polymer additive on the local entrainment process along the TNTI in the entrainment transition and enhancement regimes of a turbulent round water jet. We employ time-resolved simultaneous PIV and



https://doi.org/10.1017/jfm.2025.231 Published online by Cambridge University Press

LIF to measure the velocity and scalar concentration fields. From the scalar concentration field, we detect the TNTI and engulfed 'bubbles'. The entrainment velocity along the TNTI is determined using an interface-tracking method. By applying the spatial-filtering to the velocity and scalar concentration fields, we also analyse the geometrical feature of the TNTI and the entrainment velocity at multi-scales.

In polymer-laden water jets, polymers redistribute energy among different scales: reducing the energy content in dissipative scales and enhancing energy content in large scales. The latter induces more intermittent TNTI fluctuations in the radial direction and engulfs more bubbles into the turbulent region. Though the engulfment contribution to the total mass flux increases with $Wi$, engulfment is still not the primary entrainment mechanism in polymer-laden water jets in the present parameter range. In addition, we also note that the engulfment contribution to the total mass flux remains nearly constant in the streamwise direction. Thus, engulfment is not related to the evolution from the entrainment transition regime to the entrainment enhancement regime.

The entrainment process is then investigated from the perspective of TNTI length and local entrainment velocity at multi-scales. The local entrainment velocity is increased in both regimes, which is caused by the contribution from the polymer elastic stress and more intermittent TNTI motion. The difference between the two regimes comes from the TNTI length. In the entrainment transition regime, polymers reduce the fractal dimension of TNTI and lead to a smaller interface length, consistent with previous studies (Guimarães *et al.* 2020; Yamani *et al.* 2021; Guimarães *et al.* 2025). In the entrainment enhancement regime, the fractal dimension of TNTI as well as the interface length are not altered by polymers. This difference may be traced to the degree of polymer elasticity, with high and low elasticity in the entrainment transition and enhancement regimes, respectively. Our results also show that, in the entrainment enhancement regime, the TNTI length and mean entrainment velocity, when properly normalised, are independent of the Weissenberg number, demonstrating the universal nature of polymer-laden jet in this regime. In addition, in the entrainment enhancement regime, the normalised velocity fluctuations and mean entrainment velocity of the viscoelastic jet are higher than that of the Newtonian jet.

Based on our experimental results and previous numerical simulations (Guimarães *et al.* 2020, 2022), the transition from the entrainment reduction regime to entrainment enhancement regime for large-$Wi$ jets can be understood as follows: (i) the initial depletion of small-scale motions caused by polymers and the subsequent attenuation of this effect in the very far field, where the local $Wi$ is small; (ii) the overall enhancement of large-scale engulfment at all regions (near field and far field) that is not attenuated in the very far field.

**Acknowledgements.** We are grateful to stimulating discussions with Prof. Jinjun Wang and acknowledge Prof. Chao Sun for the rheology measurement and Jia-Qi Ma for help in PIV and LIF measurements.

**Funding.** This work is financially supported by the National Natural Science Foundation of China (NSFC) through Grant Nos. 12388101, 12125204 and 12402298, and the 111 Project of China through Grant No. B17037.

**Declaration of interests.** The authors report no conflict of interest.

## Appendix A. Viscosity of the polymer solution

The shear viscosity was measured by a Discovery HR1 rheometer (TA instruments) equipped with a cone-plate geometry. The cone is 40 mm in diameter and has an angle of 2°, allowing for the shear rate in the range $6 < \dot{\gamma} < 600\ \mathrm{s}^{-1}$. The measured viscosity $\mu$



https://doi.org/10.1017/jfm.2025.231 Published online by Cambridge University Press

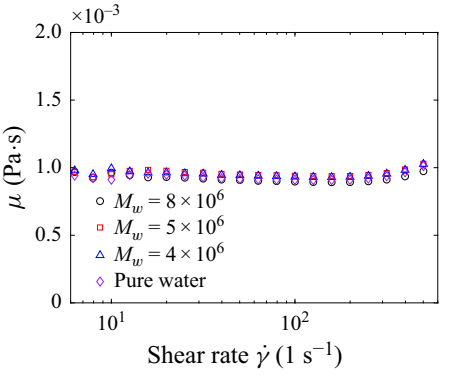



Figure 14. Measured viscosity of pure water and polymer solutions (20 ppm) used in our experiment.

at 22 °C is shown in figure 14. In our experiment, the polymer solutions are in the dilute regime and the viscosity change due to the addition of polymer additives can hardly be observed. Moreover, the viscosity remains nearly constant within the shear rate that can be realised in our rheometer. Therefore, the shear-thinning effect of polymer solutions is only marginal in our study (Deblais *et al.* 2020).

## Appendix B. Velocity and scalar statistics

Figure 15(*a*) compares the streamwise evolution of the jet half-width $b$ obtained from local PIV measurements with the full-field velocity results reported by Peng *et al.* (2023). Here, $b$ is defined as the radial distance at which the mean streamwise velocity decays to half of the local centreline value. The local PIV measured $b$ is consistent with the full-field results for both pure water and polymer solution jets. In the case of a pure water jet, $b$ scales linearly with the streamwise distance $x$, exhibiting a spreading rate $R_b \approx 0.088$ (refer to Peng *et al.* (2023) for more details). Following the approach of Guimarães *et al.* (2020), we applied a linear fit to $b$ in each local PIV measurement and $R_b$ for each position is listed in table 2. Among the four cases of polymer-laden jets measured in this study, two ($Wi = 24.6$ at $x/D = [35, 47]$ and $Wi = 36.7$ at $x/D = [50, 62]$) exhibit a spreading rate of approximately 0.117 (33 % larger compared with the pure water jet), indicating that these polymer-laden jets have entered the entrainment enhancement regime. The other two polymer-laden jets ($Wi = 36.7$ at $x/D = [35, 47]$ and $Wi = 85.6$ at $x/D = [50, 62]$) display a half-width spreading rate slightly larger than that of the pure water jet, suggesting that they are still in the transition range and have not yet entered the entrainment enhancement regime. For the $Wi = 85.6$ case, the spreading rate is clearly reduced by the polymers in the near field at $20 < x/D < 35$, in agreement with the DNS results of Guimarães *et al.* (2020) and the experiments of Yamani *et al.* (2021).

Analogous to the half-width of the velocity field, we can define the half-width $b_{\phi_R}$ of the scalar concentration field, as depicted in figure 15(*b*). In the Newtonian case, $b_{\phi_R}$ increases linearly with $x/D$, yielding a spreading rate of $R_{b_\phi} \approx 0.115$, which is in line with the value reported by Mistry *et al.* (2016). It is also observed that $R_{b_\phi}$ in the entrainment enhancement regime remains independent of $Wi$, while the positions entering this regime shift to larger $x$ values as $Wi$ increases. In the entrainment enhancement regime ($Wi = 24.6$ at $x/D = [35, 47]$ and $Wi = 36.7$ at $x/D = [50, 62]$), $R_{b_\phi} \approx 0.157$, which is approximately 36 % larger than that of the pure water case. However, in cases



https://doi.org/10.1017/jfm.2025.231 Published online by Cambridge University Press

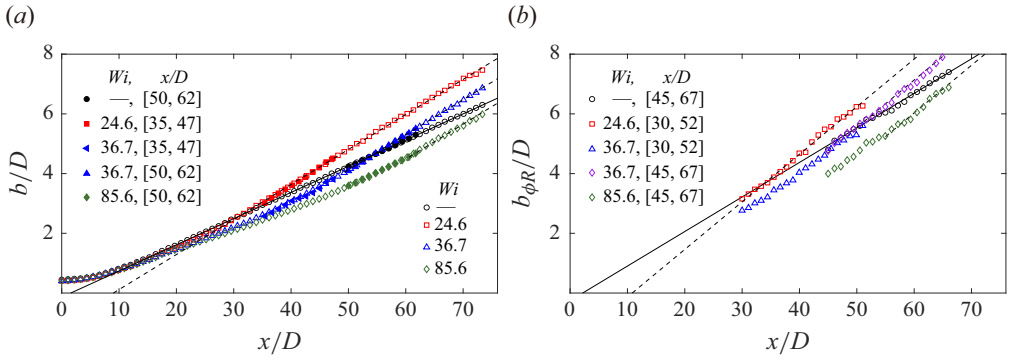



Figure 15. (*a*) Variation of the jet half-width $b$ (normalised by the pipe diameter $D$) along the flow direction for both the pure water and polymer-laden jets at different $Wi$ values. The hollow and solid symbols represent results from the full-field PIV of Peng *et al.* (2023) and local PIV in this study, respectively. The solid and dashed lines are linear fits to $b$ in the self-similar region of the pure water jet and the polymer-laden jet at $Wi = 24.6$. Dashed lines with the same slope as that of the $Wi = 24.6$ case are also shown for the $Wi = 36.7$ and 85.6 cases. (*b*) Analogous to panel (*a*), but the half-width is defined using the scalar concentration.

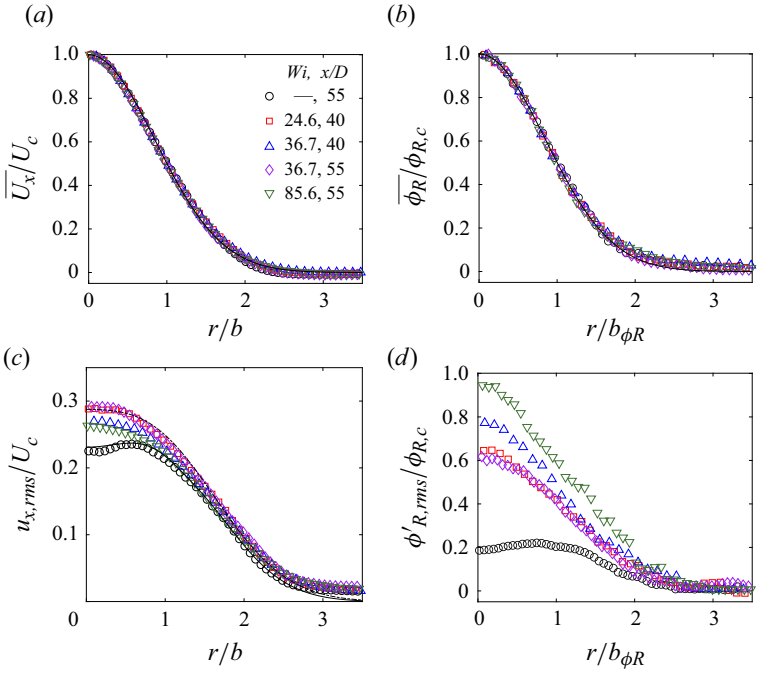



Figure 16. Radial profiles of the normalised (*a*) mean axial velocity, (*b*) mean scalar concentration, (*c*) axial velocity fluctuation and (*d*) scalar concentration fluctuation.

that are still developing ($Wi = 36.7$ at $x/D = [35, 47]$ and $Wi = 85.6$ at $x/D = [50, 62]$), $R_{b_\phi}$ values are slightly larger than that of the pure water jet.

Figure 16 presents the normalised mean and root-mean-square (r.m.s.) velocity and scalar profiles from the local PIV/LIF measurement. The velocity profiles, discussed in detail by Peng *et al.* (2023), can be summarised as follows. First, the profiles $\overline{U_x}/U_c$ (figure 16*a*) for pure water and polymer solutions at different downstream positions coincide with each other. Second, the profiles of the streamwise turbulent intensities



https://doi.org/10.1017/jfm.2025.231 Published online by Cambridge University Press

$u_{x,rms}/U_c$ (figure 16*b*) in the polymer-laden jets consistently exceed those in the pure water jet, evolving into a new self-similar state in the far field (as indicated by the black dashed line in figure 16*b*). It is evident that the $u_{x,rms}/U_c$ profiles for the polymer-laden jets at $Wi = 24.6$, $x = 40D$ and $Wi = 36.7$, $x = 55D$ collapse together in the entrainment enhancement regime.

The mean scalar concentration profiles $\phi_R/\phi_{R,c}$ of both pure water and polymer-laden jets at various $x$ values exhibit a remarkable collapse when normalised by the local scalar half-width $b_{\phi_R}$. These profiles can be approximately fitted by a Gaussian curve $\overline{\phi_R}/\phi_{R,c} = \exp(-0.69(r/b_{\phi_R})^2)$, as indicated by the black line in figure 16(*b*). Figure 16(*d*) also presents the normalised r.m.s. scalar concentration profiles, $\phi'_{R,rms}/\phi_{R,c}$, in the pure water and polymer-laden jets. Though $\phi'_{R,rms}/\phi_{R,c}$ and $u_{x,rms}/U_c$ are both enhanced in the measurement position, the degree of enhancement differs. For the $Wi = 85.6$ case, $\phi'_{R,rms}/\phi_{R,c}$ shows the largest increase, while the increase in $u_{x,rms}/U_c$ is the smallest, indicating a qualitatively different effect of polymers on the velocity and scalar. The scalar field results are in agreement with the simulation results of passive scalar mixing reported by Guimarães *et al.* (2025), providing evidence for the employment of scalar to detect TNTI in viscoelastic jet flow.

## Appendix C. Turbulent/non-turbulent interface

Various empirical methods have been proposed to detect the TNTI, including the isosurface of vorticity or velocity fluctuation (de Silva *et al.* 2013; da Silva *et al.* 2014*a*; Watanabe *et al.* 2018; Balamurugan *et al.* 2020). However, in PIV measurement near the TNTI, the particle displacement is small, resulting in large uncertainties in the measured velocity and vorticity. An alternative approach to detect TNTI is the isosurface of passive scalar, which has been extensively employed in experiments of Newtonian jet (Westerweel *et al.* 2009; Mistry *et al.* 2016; Kohan & Gaskin 2020). In Appendix B, we compare the statistics of velocity and scalar fields, showing that there are some similarities but also some differences between them. In this section, we will show that the passive scalar can still be used to detect TNTI, and introduce the method to measure the local entrainment velocity along the TNTI via time-resolved simultaneous velocity and scalar concentration fields.

### C.1 *Detection of the turbulent/non-turbulent interface*

The detection of TNTI necessitates a threshold of scalar concentration (Prasad & Sreenivasan 1989). Across the TNTI, there is a sharp jump in flow properties, including scalar concentration, kinetic energy, vorticity and energy dissipation rate. This feature can be used to determine the scalar concentration threshold (Prasad & Sreenivasan 1989; Westerweel *et al.* 2009; Mistry *et al.* 2016; Kohan & Gaskin 2020), which is achieved by a conditional average process. Given a scalar concentration threshold $\phi_{R,th}$ and a variable $f$, the mean value of $f$ is calculated using all points sampled on the FOV where the local concentration exceeds $\phi_{R,th}$,

$$\widetilde{f}(\phi_{R,th}) = \langle f \,|_{\phi_R > \phi_{R,th}} \rangle. \tag{C1}$$

Then, the threshold is chosen at the value where $\widetilde{f}(\phi_{R,th})$ exhibits a slope change. Since the jet decays along the streamwise direction, both $\phi_{R,th}$ and $f$ need to be normalised by their centreline mean values $\phi_{R,c}$ at the specific streamwise position during the conditional average. In addition, islands in the ambient fluid are not considered in this procedure (Mistry *et al.* 2016).



https://doi.org/10.1017/jfm.2025.231 Published online by Cambridge University Press

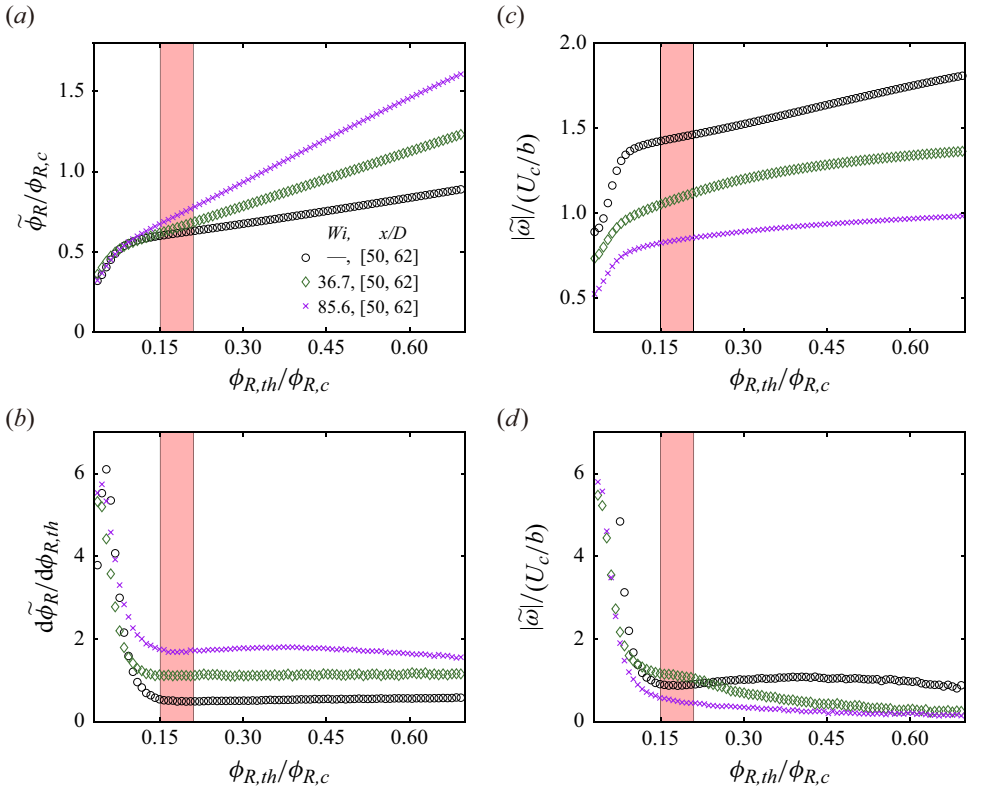



Figure 17. (*a*) Conditional averaged scalar concentration $\widetilde{\phi}_R/\phi_{R,c}$ which is averaged across all positions where $\phi_R/\phi_{R,c} > \phi_{R,th}/\phi_{R,c}$ and over the entire duration of the experiment. (*c*) Conditional average of the normalised out-of-plane vorticity magnitude $|\omega|/(U_c/b)$. The derivatives of the data in panels (*a*) and (*c*) are shown in panels (*b*) and (*d*). The red filled rectangles denote the range of TNTI concentration threshold.

The conditional averaged scalar concentration $\widetilde{\phi_R}/\phi_{R,c}$ and the out-of-plane vorticity magnitude $|\widetilde{\omega}|/U_c/b$ are shown in figure 17(*a,c*). The derivatives of these quantities with respect to $\phi_{R,th}/\phi_{R,c}$ are presented in figure 17(*b,d*). We observe that the local slopes decay with $\phi_{R,th}/\phi_{R,c}$ and then tend to around a constant value, and the transition of slope change happens around the red rectangles shown in figure 17(*b,d*). In this study, the concentration threshold is set to be $\phi_R/\phi_{R,c} = 0.18$, as in a previous study (Mistry *et al.* 2016), and the TNTI is selected as the longest continuous isocontour along this threshold. It is important to note that we have varied the threshold in the range $\phi_R/\phi_{R,c} = 0.18 \pm 0.03$ (indicated by red rectangles in figure 17) and found that the results are practically the same within error bars.

In the inset of figure 3(*a*), the green curve depicts the TNTI of the polymer-laden jet ($Wi = 85.6$) determined by the scalar concentration contour $\phi_R/\phi_{R,c} = 0.18$. This green curve effectively demarcates the turbulent and non-turbulent regions. As in Newtonian jet, we normalise $s_n$ with $\lambda$ (Gaskin 2020; da Silva & Taveira 2010; Kohan & Watanabe *et al.* 2014). The vorticity jump along $s_n$ exhibits a thickness of approximate $\lambda$, as indicated by the red rectangles in figure 3. In the case of polymer-laden jets, both the Kolmogorov length scale, $\eta$, and Taylor scale, $\lambda$, increase with $Wi$ due to the suppression of small scales. When $s_n$ is normalised by $\lambda$, the jump of $\langle|\omega|\rangle_I/(U_c/b)$ also happens within a thickness of $\lambda$. In both Newtonian and polymer-laden jets, $\lambda \approx 30\eta$. Thus, figure 3(*b*) will



https://doi.org/10.1017/jfm.2025.231 Published online by Cambridge University Press

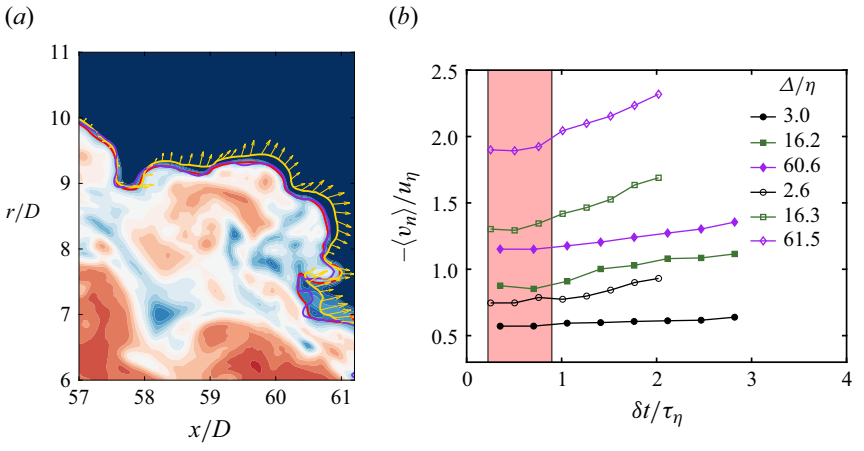



Figure 18. (*a*) Process to compute the local entrainment velocity $v_n$. The red and yellow lines represent the TNTI at $t_0$ and $t_0 + \delta t$, respectively. The yellow vectors interpolated along the yellow curve denote the local fluid velocity $\boldsymbol{u_I}$. The purple line is the shifted interface of the yellow one by a distance of $-\boldsymbol{u_I}\delta t$. (*b*) Variation of the ensemble averaged local entrainment velocity $-\langle v_n \rangle$ at different filter sizes versus $\delta t$. The filled and open symbols represent the pure water and $Wi = 36.7$ cases with comparable filter size. Within the vertical bar, $-\langle v_n \rangle$ are almost insensitive to the variation of $\delta t$.

look similar when $s_n$ is normalised by $30\eta$. Future experiments with a larger range of Reynolds number are needed to distinguish which scale is better to characterise the TNTI thickness. We note that $\langle \phi_R \rangle_I / \phi_{R,c}$ decays to the noise level almost immediately after $s_n/\lambda < 0$, resulting in a narrower thickness of scalar concentration jump (figure 3*a*).

### C.2 *Local entrainment velocity*

Wolf *et al.* (2012) proposed a 'graphical' approach to determine the local entrainment velocity $v_n$ along the TNTI by tracking the TNTI's displacement. The displacement of TNTI has two contributions: the local fluid flow advection and turbulent entrainment across the TNTI. Consequently, the spreading velocity $\boldsymbol{u_s}$ of the TNTI is the sum of the local convective velocity $\boldsymbol{u_I}$ and the local entrainment velocity $v_n$, i.e. $v_n \boldsymbol{s_n} = \boldsymbol{u_s} - \boldsymbol{u_I}$. It is worth noting that this 'graphical' method was initially applied to three-dimensional (3-D) particle-tracking data, and then extended to a two-dimensional (2-D) intersection of a 3-D interface (Mistry *et al.* 2016; Kankanwadi & Buxton 2020; Long *et al.* 2022). This was achieved by tracking the TNTI from the 2-D time-resolved scalar concentration field and simultaneous measurement of the velocity field, which provides the local advection velocity on the TNTI. Figure 18(*a*) illustrates the process to compute $v_n$. Specifically, the TNTIs, identified at two moments $t_0$ and $t_0 + \delta t$ ($\delta t$ is a short time interval and the proper choice of $\delta t$ is discussed later) are represented by the red and yellow curves, respectively. The contribution from local advection is subtracted by shifting the TNTI at $t_0 + \delta t$ by a distance $-\boldsymbol{u_I}\delta t$ (see the purple curve in figure 18*a*). The local entrainment velocity is then obtained by dividing the local normal distance from the red curve to the purple curve by the time interval $\delta t$. Note that the positive TNTI normal direction, i.e. $s_n > 0$, points to the turbulent region (see figure 3*a*), so that $v_n < 0$ signifies entrainment, while $v_n > 0$ indicates detrainment. The $v_n$ obtained in our study is the projection of the entrainment velocity onto the $x-r$ plane.

To study the entrainment process at multi-scales, we eliminated small-scale fluctuations of the velocity and scalar concentration fields below a certain filter size, denoted as $\Delta$, by convolving them with a filter $G_\Delta$. This method is commonly used in the TNTI studies



https://doi.org/10.1017/jfm.2025.231 Published online by Cambridge University Press

(Mistry *et al.* 2016; Xu *et al.* 2023). The box-averaging filter $G_\Delta$ employed here is defined as follows:

$$G_\Delta = \begin{cases} 0, & |r| \geqslant \Delta/2, \\ 1/\Delta^2, & |r| < \Delta/2. \end{cases} \tag{C2}$$

The aforementioned 'graphical' method can then be applied to the filtered scalar concentration and velocity fields to obtain $v_n(\Delta)$ at scale $\Delta$. In the 'graphical' method, it is crucial to choose an appropriate time interval $\delta t$ to minimise random errors in LIF/PIV measurements and the effect of out-of-plane motion. In this study, we adopt an empirical method akin to that used by Long *et al.* (2022) and Mistry *et al.* (2016). In short, an appropriate $\delta t$ is chosen when the ensemble averaged local entrainment velocity, $\langle v_n \rangle$, remains almost invariant when the time interval is varied around the determined $\delta t$. Figure 18(*b*) shows $\langle v_n \rangle$ versus $\delta t$ over the range $0.2 < \delta t/\tau_\eta < 3$. We observe that $\langle v_n \rangle$ is insensitive to $\delta t$ when $0.2 < \delta t/\tau_\eta < 0.9$, as marked by the red vertical bar. We hence choose $\delta_t = 5$ ms ($\sim 1\tau_\eta$) for all the experiments in this study across all filter sizes.

## References


Abreu, H., Pinho, F.T. & da Silva, C.B. 2022 Turbulent entrainment in viscoelastic fluids. *J. Fluid Mech.* **934**, A36.

Bailey, F.E. & Koleske, J.V. 1976 *Poly (ethylene oxide)*. Academic Press.

Baj, P., Bruce, P.J.K. & Buxton, O.R.H. 2016 On a PLIF quantification methodology in a nonlinear dye response regime. *Exp. Fluids* **57** (6), 1–19.

Balamurugan, G., Rodda, A., Philip, J. & Mandal, A.C. 2020 Characteristics of the turbulent non-turbulent interface in a spatially evolving turbulent mixing layer. *J. Fluid Mech.* **894**, A4.

Boffetta, G., Mazzino, A. & Musacchio, S. 2011 Effects of polymer additives on Rayleigh–Taylor turbulence. *Phys. Rev. E* **83** (5), 056318.

Boffetta, G., Mazzino, A., Musacchio, S. & Vozella, L. 2010 Polymer heat transport enhancement in thermal convection: the case of Rayleigh–Taylor turbulence. *Phys. Rev. Lett.* **104** (18), 184501.

Boulafentis, T., Lacassagne, T., Cagney, N. & Balabani, S. 2024 Coherent structures of elastoinertial instabilities in Taylor–Couette flows. *J. Fluid Mech.* **986**, A27.

Cai, W.-H., Li, F.-C. & Zhang, H.-N. 2010 Dns study of decaying homogeneous isotropic turbulence with polymer additives. *J. Fluid Mech.* **665**, 334–356.

Cocconi, G., De Angelis, E., Frohnapfel, B., Baevsky, M. & Liberzon, A. 2017 Small scale dynamics of a shearless turbulent/non-turbulent interface in dilute polymer solutions. *Phys. Fluids* **29** (7), 075102.

Crimaldi, J.P. 2008 Planar laser induced fluorescence in aqueous flows. *Exp. Fluids* **44** (6), 851–863.

Deblais, A., Herrada, M.A., Eggers, J. & Bonn, D. 2020 Self-similarity in the breakup of very dilute viscoelastic solutions. *J. Fluid Mech.* **904**, R2.

Guimarães, M.C., Pimentel, N., Pinho, F.T. & da Silva, C.B. 2020 Direct numerical simulations of turbulent viscoelastic jets. *J. Fluid Mech.* **899**, A11.

Guimarães, M.C., Pinho, F.T. & da Silva, C.B. 2022 Turbulent planar wakes of viscoelastic fluids analysed by direct numerical simulations. *J. Fluid Mech.* **946**, A26.

Guimarães, M.C., Pinho, F.T. & da Silva, C.B. 2023 Viscoelastic jet instabilities studied by direct numerical simulations. *Phys. Rev. Fluids* **8** (10), 103301.

Guimarães, M.C., Pinho, F.T. & da Silva, C.B. 2024 The similarity theory of free turbulent shear flows of viscoelastic fluids. *J. Non-Newtonian Fluid Mech.* **323**, 105148.

Guimarães, M.C., Pinho, F.T. & da Silva, C.B. 2025 Mixing of passive scalars in viscoelastic turbulent jets and wakes. *Phys. Rev. Fluids* **10** (2), 023303.

Gupta, V.K., Sureshkumar, R. & Khomami, B. 2005 Passive scalar transport in polymer drag-reduced turbulent channel flow. *AIChE J.* **51** (7), 1938–1950.

Holzner, M., Liberzon, A., Nikitin, N., Lüthi, B., Kinzelbach, W. & Tsinober, A. 2008 A Lagrangian investigation of the small-scale features of turbulent entrainment through particle tracking and direct numerical simulation. *J. Fluid Mech.* **598**, 465–475.

Holzner, M. & Lüthi, B. 2011 Laminar superlayer at the turbulence boundary. *Phys. Rev. Lett.* **106** (13), 134503.




https://doi.org/10.1017/jfm.2025.231 Published online by Cambridge University Press

JAHANBAKHSHI, R. & MADNIA, C.K. 2016 Entrainment in a compressible turbulent shear layer. *J. Fluid Mech.* **797**, 564–603.

KANKANWADI, K.S. & BUXTON, O.R.H. 2020 Turbulent entrainment into a cylinder wake from a turbulent background. *J. Fluid Mech.* **905**, A35.

KOHAN, K.F. & GASKIN, S. 2020 The effect of the geometric features of the turbulent/non-turbulent interface on the entrainment of a passive scalar into a jet. *Phys. Fluids* **32** (9), 095114.

KRUG, D., HOLZNER, M., LÜTHI, B., WOLF, M., KINZELBACH, W. & TSINOBER, A. 2015 The turbulent/non-turbulent interface in an inclined dense gravity current. *J. Fluid Mech.* **765**, 303–324.

LAVOIE, P., AVALLONE, G., DE GREGORIO, F., ROMANO, G.P. & ANTONIA, R.A. 2007 Spatial resolution of piv for the measurement of turbulence. *Exp. Fluids* **43** (1), 39–51.

LIBERZON, A., HOLZNER, M., LÜTHI, B., GUALA, M. & KINZELBACH, W. 2009 On turbulent entrainment and dissipation in dilute polymer solutions. *Phys. Fluids* **21** (3), 035107.

LONG, Y.G., WANG, J.J. & PAN, C. 2022 Universal modulations of large-scale motions on entrainment of turbulent boundary layers. *J. Fluid Mech.* **941**, A68.

MATHEW, J. & BASU, A.J. 2002 Some characteristics of entrainment at a cylindrical turbulence boundary. *Phys. Fluids* **14** (7), 2065–2072.

MENEVEAU, C. & SREENIVASAN, K.R. 1990 Interface dimension in intermittent turbulence. *Phys. Rev. A* **41** (4), 2246–2248.

MISTRY, D., PHILIP, J. & DAWSON, J.R. 2019 Kinematics of local entrainment and detrainment in a turbulent jet. *J. Fluid Mech.* **871**, 896–924.

MISTRY, D., PHILIP, J., DAWSON, J.R. & MARUSIC, I. 2016 Entrainment at multi-scales across the turbulent/non-turbulent interface in an axisymmetric jet. *J. Fluid Mech.* **802**, 690–725.

MOAZZEN, M., LACASSAGNE, T., THOMY, V. & BAHRANI, S.A. 2023 Friction dynamics of elasto-inertial turbulence in Taylor–Couette flow of viscoelastic fluids. *Phil. Trans. R. Soc. Lond. A* **381** (2246), 20220300.

MORTON, B.R., TAYLOR, G.I. & TURNER, J.S. 1956 Turbulent gravitational convection from maintained and instantaneous sources. *Proc. R. Soc. Lond. A* **234** (1196), 1–23.

NIE, S., CHIU, D.T. & ZARE, R.N. 1994 Probing individual molecules with confocal fluorescence microscopy. *Science* **266** (5187), 1018–1021.

OUELLETTE, N.T., XU, H.-T. & BODENSCHATZ, E. 2009 Bulk turbulence in dilute polymer solutions. *J. Fluid Mech.* **629**, 375–385.

OXLADE, A.R., VALENTE, P.C., GANAPATHISUBRAMANI, B. & MORRISON, J.F. 2012 Denoising of time-resolved PIV for accurate measurement of turbulence spectra and reduced error in derivatives. *Exp. Fluids* **53** (5), 1561–1575.

PARKER, D.A., BURRIDGE, H.C., PARTRIDGE, J.L. & LINDEN, P.F. 2020 A comparison of entrainment in turbulent line plumes adjacent to and distant from a vertical wall. *J. Fluid Mech.* **882**, A4.

PENG, S.-H., ZHANG, Y.-B. & XI, H.-D. 2023 Effects of polymer additives on the entrainment of turbulent water jet. *Phys. Fluids* **35** (4), 045110.

PHILIP, J., MENEVEAU, C., DE SILVA, C.M. & MARUSIC, I. 2014 Multiscale analysis of fluxes at the turbulent/non-turbulent interface in high Reynolds number boundary layers. *Phys. Fluids* **26** (1), 015105.

POLMAR, N. & MOORE, K.J. 2004 *Cold War Submarines: the Design and Construction of US and Soviet Submarines*. Potomac Books, Inc.

PRASAD, R.R. & SREENIVASAN, K.R. 1989 Scalar interfaces in digital images of turbulent flows. *Exp. Fluids* **7** (4), 259–264.

RAY, P.K. & ZAKI, T.A. 2014 Absolute instability in viscoelastic mixing layers. *Phys. Fluids* **26** (1), 014103.

RAY, P.K. & ZAKI, T.A. 2015 Absolute/convective instability of planar viscoelastic jets. *Phys. Fluids* **27** (1), 014110.

UR REHMAN, S., LEE, J. & LEE, C. 2022 Effect of Weissenberg number on polymer-laden turbulence. *Phys. Rev. Fluids* **7** (6), 064303.

ROSHKO, A. 1976 Structure of turbulent shear flows: a new look. *AIAA J.* **14** (10), 1349–1357.

ROSTI, M.E., PERLEKAR, P. & MITRA, D. 2023 Large is different: nonmonotonic behavior of elastic range scaling in polymeric turbulence at large Reynolds and Deborah numbers. *Sci. Adv.* **9** (11), eadd3831.

DA SILVA, C.B., HUNT, J.C.R., EAMES, I. & WESTERWEEL, J. 2014*a* Interfacial layers between regions of different turbulence intensity. *Annu. Rev. Fluid Mech.* **46** (1), 567–590.

DA SILVA, C.B. & TAVEIRA, R.R. 2010 The thickness of the turbulent/nonturbulent interface is equal to the radius of the large vorticity structures near the edge of the shear layer. *Phys. Fluids* **22** (12), 121702.

DA SILVA, C.B., TAVEIRA, R.R. & BORRELL, G. 2014*b* Characteristics of the turbulent/nonturbulent interface in boundary layers, jets and shear-free turbulence. Journal of Physics: Conference Series, vol. 506, pp. 012015. IOP Publishing.



https://doi.org/10.1017/jfm.2025.231 Published online by Cambridge University Press

DE SILVA, C.M., PHILIP, J., CHAUHAN, K., MENEVEAU, C. & MARUSIC, I. 2013 Multiscale geometry and scaling of the turbulent-nonturbulent interface in high Reynolds number boundary layers. *Phys. Rev. Lett.* **111** (4), 044501.

SOLIGO, G. & ROSTI, M.E. 2023 Non-Newtonian turbulent jets at low-Reynolds number. *Intl J. Multiphase Flow* **167**, 104546.

VAITHIANATHAN, T., ROBERT, A., BRASSEUR, J.G. & COLLINS, L.R. 2007 Polymer mixing in shear-driven turbulence. *J. Fluid Mech.* **585**, 487–497.

VALENTE, P.C., DA SILVA, C.B. & PINHO, F.T. 2014 The effect of viscoelasticity on the turbulent kinetic energy cascade. *J. Fluid Mech.* **760**, 39–62.

VALENTE, P.C., DA SILVA, C.B. & PINHO, F.T. 2016 Energy spectra in elasto-inertial turbulence. *Phys. Fluids* **28** (7), 075108.

VONLANTHEN, R. & MONKEWITZ, P.A. 2013 Grid turbulence in dilute polymer solutions: PEO in water. *J. Fluid Mech.* **730**, 76–98.

WATANABE, T., SAKAI, Y., NAGATA, K., ITO, Y. & HAYASE, T. 2014 Enstrophy and passive scalar transport near the turbulent/non-turbulent interface in a turbulent planar jet flow. *Phys. Fluids* **26** (10), 105103.

WATANABE, T., ZHANG, X. & NAGATA, K. 2018 Turbulent/non-turbulent interfaces detected in dns of incompressible turbulent boundary layers. *Phys. Fluids* **30** (3), 035102.

WEI, M.-H., LI, B., DAVID, R.L.A., JONES, S.C., SAROHIA, V., SCHMITIGAL, J.A. & KORNFIELD, J.A. 2015 Megasupramolecules for safer, cleaner fuel by end association of long telechelic polymers. *Science* **350** (6256), 72–75.

WESTERWEEL, J., FUKUSHIMA, C., PEDERSEN, J.M. & HUNT, J.C.R. 2009 Momentum and scalar transport at the turbulent/non-turbulent interface of a jet. *J. Fluid Mech.* **631**, 199–230.

WHITE, C.M. & MUNGAL, M.G. 2008 Mechanics and prediction of turbulent drag reduction with polymer additives. *Annu. Rev. Fluid Mech.* **40** (1), 235–256.

WOLF, M., LÜTHI, B., HOLZNER, M., KRUG, D., KINZELBACH, W. & TSINOBER, A. 2012 Investigations on the local entrainment velocity in a turbulent jet. *Phys. Fluids* **24** (10), 105110.

XI, H.-D., BODENSCHATZ, E. & XU, H.T. 2013 Elastic energy flux by flexible polymers in fluid turbulence. *Phys. Rev. Lett.* **111** (2), 024501.

XI, L. 2019 Turbulent drag reduction by polymer additives: fundamentals and recent advances. *Phys. Fluids* **31** (12), 121302.

XU, C.Y., LONG, Y.G. & WANG, J.J. 2023 Entrainment mechanism of turbulent synthetic jet flow. *J. Fluid Mech.* **958**, A31.

XU, D. & CHEN, J. 2013 Accurate estimate of turbulent dissipation rate using PIV data. *Exp. Therm. Fluid Sci.* **44**, 662–672.

YAMANI, S., KESHAVARZ, B., RAJ, Y., ZAKI, T.A., MCKINLEY, G.H. & BISCHOFBERGER, I. 2021 Spectral universality of elastoinertial turbulence. *Phys. Rev. Lett.* **127** (7), 074501.

YAMANI, S., RAJ, Y., ZAKI, T.A., MCKINLEY, G.H. & BISCHOFBERGER, I. 2023 Spatiotemporal signatures of elastoinertial turbulence in viscoelastic planar jets. *Phys. Rev. Fluids* **8** (6), 064610.

ZHANG, Y.-B., BODENSCHATZ, E., XU, H. & XI, H.-D. 2021 Experimental observation of the elastic range scaling in turbulent flow with polymer additives. *Sci. Adv.* **7** (14), eabd3525.

ZHANG, Y.-B. & XI, H.-D. 2022 Measured energy injection, transfer, and dissipation rates in the bulk of dilute polymeric turbulent flow: the concentration and Weissenberg number effects. *Phys. Fluids* **34** (7), 075114.

https://doi.org/10.1017/jfm.2025.231 Published online by Cambridge University Press